# 3. Transition Path Theory for Diffusion Processes

As explained in the introduction of this thesis, Transition Path Theory (TPT) provides a powerful framework to describe the statistical properties of the ensemble of reactive trajectories. In this chapter, we will recall the theoretical aspects of TPT in the context of Markov diffusion processes (Sect. 3.1) and, in particular, we will derive the main objects of TPT for the case of the Smoluchowski dynamics (Sect. 3.2) and for the Langevin dynamics (Sect. 3.3), respectively. The remainder of this chapter is devoted to illustrate TPT via several low dimensional examples where we will also explain briefly how the various quantities of TPT were computed on the simple examples. For the details of the numerical considerations, especially how we numerically solved the committor equation see Section A.1 in the Appendix. For more details, we refer the reader to the original references [34, 92, 65].

## 3.1. Theory: Transition Path Theory

Consider a system whose dynamics is governed by the following stochastic differential equation

$$\mathrm{d}X_t = b(X_t)\mathrm{d}t + \sigma \mathrm{d}W_t, \tag{3.1}$$

where $X_t \in \mathbb{R}^d$, $b(x) = (b_1(x), \ldots, b_d(x))^T \in \mathbb{R}^d$ is the drift vector, $\sigma \in \mathbb{R}^{d\times d}$ is a real matrix and $W_t$ is a $d$-dimensional, standard Wiener process. The generator associated with the dynamics (3.1) is given by

$$\begin{aligned} \mathcal{L}_{bw}u(x) &= \sum_{i,j=1}^{d} a_{ij}\frac{\partial^2 u(x)}{\partial x_i \partial x_j} + \sum_{i=1}^{d} b_i(x)\frac{\partial u(x)}{\partial x_i} \\ &= a : \nabla\nabla u(x) + b(x)\cdot\nabla u(x), \end{aligned} \tag{3.2}$$

where $a = \frac{1}{2}\sigma\sigma^T$ is the diffusion matrix.

### 3.1.1. Ensemble of Reactive Trajectories

Let $X(t), -\infty < t < \infty$ be an infinity long trajectory solution of (3.1) which is ergodic with respect to the equilibrium probability density function $\rho(x)$, i.e. given any suitable observable $\phi(x)$, we have

$$\lim_{T\to\infty}\frac{1}{2T}\int_{-T}^{T}\phi(X(t))\mathrm{d}t = Z^{-1}\int_{\mathbb{R}^d}\phi(x)\rho(x)\mathrm{d}x, \tag{3.3}$$

where $Z = \int_{\mathbb{R}^d}\rho(x)\mathrm{d}x$. (3.3) is a property of any generic trajectory in the system which, during the time-interval $[-T, T]$, will be involved in any given reaction many

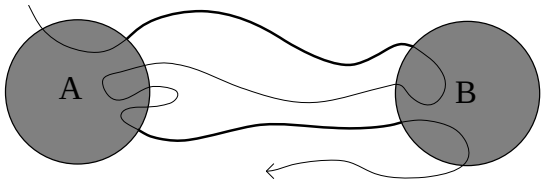


Figure 3.1.: Schematic representation of the reactant state $A$, the product state $B$ and a piece of an equilibrium trajectory (shown in thin black). The subpieces connecting $\partial A$ to $\partial B$ (shown in thick black) are each a reactive trajectory, and the collection of all of them is the ensemble of reactive trajectories.

times when $T$ is large (and infinitely often as $T \to \infty$). Suppose however that one is not interested in the statistical properties of such a generic trajectory, but rather in the statistical properties that this trajectory displays while involved in a reaction. This question can be made precise as follows. Suppose that $A \subset \mathbb{R}^d$ and $B \subset \mathbb{R}^d$ are two regions in configuration space that characterize the system while it is in the reactant and the product states, respectively, of a given reaction. Then, given any generic trajectory, $x(t)$, $-\infty < t < \infty$, we can prune this trajectory as illustrated in Figure 3.1 to consider only the pieces of this trajectory that connect $\partial A$ (the boundary of $A$) to $\partial B$ (the boundary of $B$). Each such piece is a reactive trajectory and the collection of all of them is the ensemble of reactive trajectories. By ergodicity, the statistical properties of this ensemble are independent of the particular trajectory used to generate the ensemble, and these properties are the object of TPT.

Formally, the ensemble of reactive trajectories is defined in

**Definition 3.1.1** (ensemble of reactive trajectories)**.**

$$\begin{gathered} \textit{ensemble of reactive trajectories} \\ = \{X(t) : t \in \mathcal{R}\} \textit{ where } t \in \mathcal{R} \textit{ if and only if} \\ X(t) \notin A \cup B,\ X(t^+_{AB}(t)) \in B \textit{ and } X(t^-_{AB}(t)) \in A \end{gathered} \tag{3.4}$$

*where*

$$\begin{aligned} t^+_{AB}(t) &= \textit{smallest } t' \geq t \textit{ such that } X(t') \in A \cup B, \\ t^-_{AB}(t) &= \textit{largest } t' \leq t \textit{ such that } X(t') \in A \cup B. \end{aligned} \tag{3.5}$$

Each continuous piece of the trajectory going from $A$ to $B$ in the ensemble (3.1.1) is a specific reactive trajectory. The main objects of TPT are then defined in terms of the reactive trajectories and expressed in terms of $\rho(x)$ and the committor functions $q(x)$ and $q_b(x)$ which will be defined in the next section.

### 3.1.2. Committor Function

We will see in the next sections that the *forward committor function* $q(x)$, defined as the probability that the trajectory starting from $x \notin A \cup B$ reaches first $B$ rather than $A$ and the *backward committor function* $q_b(x)$, defined as the probability that the trajectory arriving at $x \notin A \cup B$ came rather from $A$ than from $B$ are the crucial objects to express, e.g., the probability density function of reactive trajectories.

Formally, the forward committor function $q(x)$ satisfies the backward Kolmogorov equation associated with (3.1):

$$\begin{cases} \mathcal{L}_{bw} q = 0 & \text{in } \mathbb{R}^d \setminus (A \cup B), \\ q = 0 & \text{on } \partial A, \\ q = 1 & \text{on } \partial B, \end{cases} \tag{3.6}$$

where $\mathcal{L}_{bw}$ is the operator in (3.2). To see (3.6) notice that the committor function $q(x)$ can be expressed in terms of a conditional expectation, i.e,

$$q(x) = \mathbb{E}_x \left[ \mathbf{1}_B(X(\tau_{A\cup B})) \right],$$

where $\tau_{A\cup B}$ is the first hitting time of the process $X_t$ with respect to the set $A \cup B$. If we define the auxiliary function $g : \partial A \cup \partial B \to \mathbb{R}$ by

$$g(x) = \begin{cases} 0, & \text{if } x \in \partial A \\ 1, & \text{if } x \in \partial B \end{cases}$$

and set $f \equiv 0$ then by virtue of Theorem 2.1.3 follows that if (3.6) possesses a (classical) solution, say $u(x)$, then we have $q \equiv u$, and therefore, $q(x)$ satisfies (3.6). For conditions on the differential operator $\mathcal{L}_{bw}$ and the boundary of the set $A \cup B$ which ensure the existence of a classical solution, see Theorem 2.1.4.

A similar reasoning as above shows that the backward committor function $q_b(x)$ satisfies the backward Kolmogorov equation associated with the reversed-time process (cf. Sect. 2.1.4):

$$\begin{cases} \mathcal{L}^R_{bw} q_b = 0 & \text{in } \mathbb{R}^d \setminus (A \cup B), \\ q_b = 1 & \text{on } \partial A, \\ q_b = 0 & \text{on } \partial B, \end{cases} \tag{3.7}$$

where

$$\mathcal{L}^R_{bw} q_b = a : \nabla\nabla q_b(x) + b^R(x) \cdot \nabla q_b(x) \tag{3.8}$$

with the drift field (cf. Theorem A.6.2)

$$b^R(x) = -b(x) + \frac{2}{\rho(x)} div\big(a(x)\rho(x)\big).$$

Notice that if the process $X_t$ is reversible than in particular we have $\mathcal{L}_{bw} \equiv \mathcal{L}^R_{bw}$ and it follows that the backward committor function $q_b(x)$ can be expressed in terms of the forward committor function:

$$q_b(x) = 1 - q(x). \tag{3.9}$$

In large dimensional systems, the main question of interest then becomes how to solve (3.6), which is a highly nontrivial problem since (3.6) involves a partial differential equation for a function of many variables. The string method is a way to deal with this issue. In the context of the two-dimensional examples considered in this chapter, however, standard numerical techniques based on discretizing (3.6) by finite differences can be applied, as briefly explained in detail in the Appendix, Section A.1.

**Remark 3.1.2.** *Let $r(x)$ denote the* ***mean first passage time*** *(mean first hitting time) of the process $X_t$ with respect to the set $\mathcal{S} \subset \mathbb{R}^d$, conditional on $X(0) = x$. Formally, $r(x)$ is given by*

$$r(x) = \mathbb{E}_x[\tau_{\mathcal{S}}],$$

*where $\tau_{\mathcal{S}}$ is the hitting time of the process $X_t$ with respect to the set $\mathcal{S}$. If we set $g \equiv 0$ and $f \equiv -1$ then a similar reasoning as for the committor function shows that $r(x)$ satisfies*

$$\begin{cases} \mathcal{L}_{bw} r = -1 & \text{in } \mathbb{R}^d \setminus \mathcal{S}, \\ r = 0 & \text{on } \partial\mathcal{S}, \end{cases} \tag{3.10}$$

*where $\mathcal{L}_{bw}$ is the operator in (3.2).*

### 3.1.3. Probability Density Function of Reactive Trajectories

Let $A \subset \mathbb{R}^d$ and $B \subset \mathbb{R}^d$ denote the reactant and product states, respectively. What is the probability density to observe a reactive trajectory at position $x \notin A \cup B$ at time $t$, conditional on it being reactive at time $t$?

Intuitively, it should be clear that the probability density to observe any reactive trajectory is given by the probability density to observe any trajectory (reactive or not) at point $x$, which is $\rho(x)$, times the probability $q_b(x)$ that the trajectory came rather from $A$ than from $B$ and times the probability $q(x)$ that the trajectory reaches first $B$ rather than $A$.

Formally, the probability density function of reactive trajectories $\rho_{AB}(x)$ is defined such that, giving any observable $\phi(x)$, we have

$$\lim_{T\to\infty} \frac{\int_{\mathcal{R}\cap[-T,T]} \phi(X(t))\mathrm{d}t}{\int_{\mathcal{R}\cap[-T,T]} \mathrm{d}t} = \int_{\Omega_{AB}} \phi(x)\rho_{AB}(x)\mathrm{d}x, \tag{3.11}$$

where $\Omega_{AB} = \mathbb{R}^d \setminus (A \cup B)$. Indeed, it is proven in [34] that by exploiting both ergodicity and the strong Markov property of the dynamics the intuitive picture is right, namely that $\rho_{AB}(x)$ can be expressed in terms of $\rho(x)$, $q(x)$ and $q_b(x)$ as

$$\rho_{AB}(x) = Z_{AB}^{-1} q(x) q_b(x) \rho(x), \tag{3.12}$$

where the normalization constant $Z_{AB}$,

$$Z_{AB} = \int_{\Omega_{AB}} q(x) q_b(x) \rho(x) \mathrm{d}x, \tag{3.13}$$

is the total probability to encounter a reactive trajectory.

### 3.1.4. Probability Current and Transition Rate

The probability density $\rho_{AB}(x)$ is not the only quantity of interest as it may not be sufficient to characterize the reaction pathway. To get a better understanding of this pathway, we may also ask about the probability current of reactive trajectories. Roughly, this current is such that, integrated over any surface in $\Omega_{AB}$, it gives the probability flux of reactive trajectories across this surface, that is, the net balance

between the number of trajectories that cross this surface in one direction minus the number of them that cross this surface in the opposite direction during an infinitesimal time-interval.

More precisely, the probability current $J_{AB}(x)$ of reactive trajectories is the vector field defined in $\Omega_{AB}$ such that given any surface $\partial\mathcal{S}$ which is the boundary of a region $\mathcal{S} \subset \Omega_{AB}$, we have

$$\begin{aligned}\lim_{s\to 0^+}\frac{1}{s}\lim_{T\to\infty}\frac{1}{2T}\int_{\mathcal{R}\cap[-T,T]}&\big(\mathbf{1}_{\mathcal{S}}(X(t))\mathbf{1}_{\mathbb{R}^d\setminus\mathcal{S}}(X(t+s))\\ &-\mathbf{1}_{\mathbb{R}^d\setminus\mathcal{S}}(X(t))\mathbf{1}_{\mathcal{S}}(X(t+s))\big)\mathrm{d}t\\ =\int_{\partial\mathcal{S}}&\hat{n}_{\partial\mathcal{S}}(x)\cdot J_{AB}(x)\mathrm{d}\sigma_{\partial\mathcal{S}}(x),\end{aligned} \tag{3.14}$$

where $\hat{n}_{\partial\mathcal{S}}(x)$ is the unit normal on $\partial\mathcal{S}$ pointing outward $\mathcal{S}$ and $\mathrm{d}\sigma_{\partial\mathcal{S}}(x)$ is the surface element on $\partial\mathcal{S}$. We want to emphasize that $J_{AB}(x)$ is independent of the surface $\partial\mathcal{S}$. As shown in Section A.4 in the Appendix, $J_{AB}(x)$ can be expressed componentwise as

$$\begin{aligned}J_{AB,i}(x) = q(x)q_b(x)J_i(x)&\\ + q_b(x)\rho(x)\sum_{j=1}^{d}a_{ij}(x)\frac{\partial q(x)}{\partial x_j}&\\ - q(x)\rho(x)\sum_{j=1}^{d}a_{ij}(x)\frac{\partial q_b(x)}{\partial x_j},&\end{aligned} \tag{3.15}$$

where $J(x) = (J_1(x), \ldots, J_d(x))^T$ is the equilibrium probability current (recall that $\rho(x)$ is the equilibrium probability density function of the process):

$$J_i(x) = b_i(x)\rho(x) - \sum_{j=1}^{d}\frac{\partial}{\partial x_j}(a_{ij}(x)\rho(x)). \tag{3.16}$$

The current $J_{AB}(x)$ is divergence free, and its integral over any dividing surface $\partial\mathcal{S} \subset \Omega_{AB}$ gives the reaction rate:

$$k_{AB} = \int_{\partial\mathcal{S}}\hat{n}_{\partial\mathcal{S}}(x)\cdot J_{AB}(x)\mathrm{d}\sigma_{\partial\mathcal{S}}(x), \tag{3.17}$$

where $\hat{n}_{\partial\mathcal{S}}(x)$ is the unit normal to $\partial\mathcal{S}$ pointing toward $B$. Letting $N_T^R$ be the number of reactive trajectories observed during the time interval $[-T, T]$ in the ensemble of reactive trajectories, $k_{AB}$ is the limit

$$k_{AB} = \lim_{T\to\infty}\frac{N_T^R}{2T}, \tag{3.18}$$

i.e. it gives the exact mean frequency at which the reactive trajectories are observed within a given trajectory.

The expression (3.17) for the rate can be simplified and transformed into a volume integral over $\Omega_{AB}$:

$$k_{AB} = \int_{\Omega_{AB}}\rho(x)\sum_{i,j=1}^{d}a_{ij}(x)\frac{\partial q(x)}{\partial x_i}\frac{\partial q(x)}{\partial x_j}\mathrm{d}x. \tag{3.19}$$

For a derivation of (3.19) see Section A.4 in the Appendix.

### 3.1.5. Transition Tubes

Another quantity of interest which can be extracted from the probability current of reactive trajectories are the streamlines of this current. These are the solutions of

$$\frac{dx_i(\tau)}{d\tau} = J_{AB,i}(x(\tau)). \tag{3.20}$$

(The "time" $\tau$ in this equation is artificial and unrelated to the physical time $t$). Solving (3.20) with the initial condition $x(0) \in \partial A$ one obtains a streamline connecting $A$ to $B$; the ensemble of streamlines associated with all initial conditions $x(0) \in \partial A$ forms a bundle of curves in $\Omega_{AB}$ whose union is $\Omega_{AB}$ itself. The streamlines of the current are an indicator of the average trend of the reactive trajectories, and they allow to define reaction (or transition) tubes connecting $A$ to $B$ carrying a certain percentage of the probability flux of reactive trajectories. Indeed, suppose that $\partial' A \subset \partial A$ is a subset of the boundary of the reactant state $A$ across which $p\%$ of the probability flux of reactive trajectories go, i.e.

$$\begin{aligned} &\int_{\partial' A} \hat{n}_{\partial A}(x) \cdot J_{AB}(x) \mathrm{d}\sigma_{\partial A}(x) \\ &\quad = \frac{p}{100} \int_{\partial A} \hat{n}_{\partial A}(x) \cdot J_{AB}(x) \mathrm{d}\sigma_{\partial A}(x) \equiv \frac{p}{100} k_{AB}, \end{aligned} \tag{3.21}$$

where we used (3.29) and the fact that $\partial A$ is a dividing surface between $A$ and $B$. Then, the ensemble of streamlines obtained by solving (3.20) for all initial conditions $x(0) \in \partial' A$ forms a reaction tube connecting $A$ and $B$ which carries $p\%$ of the probability flux of reactive trajectories. Sometimes, a rather localized tube can be found which carries a high percentage of the flux: then, the reactive trajectories must remain inside this tube with high probability, i.e. it is the preferred channel for the reaction.

## 3.2. TPT in the Smoluchowski Case

In this section we summarize the objects of TPT for a system which is governed by the Smoluchowski dynamics introduced in Section 2.1.10:

$$\dot{x}_i(t) = -\gamma_i^{-1} \frac{\partial V(x(t))}{\partial x_i} + \sqrt{2\beta^{-1}\gamma_i^{-1}}\, \eta_i(t), \tag{3.22}$$

where $x = (x_1, x_2, \ldots, x_d) \in \mathbb{R}^d$ denotes the position of the particles, $V(x)$ is the potential, $\gamma_i$ is the friction coefficient on $x_i$, $\beta$ is the inverse temperature and $\eta_i(t)$ is a white noise.

Recalling that the backward generator of the Smoluchowski dynamics in (3.22) takes the form

$$\mathcal{L}_{bw} u = \beta^{-1} \Gamma^{-1} : \nabla\nabla u - \Gamma^{-1} \nabla V \cdot \nabla u, \tag{3.23}$$

the forward committor function $q(x)$ satisfies the committor equation [29] (see also

Theorem 2.1.4)

$$\begin{cases} 0 = \mathcal{L}_{bw} q \\ \quad = \beta^{-1}\Gamma^{-1} : \nabla\nabla q - \Gamma^{-1}\nabla V \cdot \nabla q & \text{in } \Omega_{AB} = \mathbb{R}^d \setminus (A \cup B), \\ q = 0 & \text{on } \partial A, \\ q = 1 & \text{on } \partial B, \end{cases} \tag{3.24}$$

where $\Gamma^{-1} = \mathrm{diag}(\gamma_1^{-1}, \ldots, \gamma_d^{-1})$. Since the Smoluchowski dynamics is reversible, the backward committor function is given via the relation in (3.9). The probability density to observe a reactive trajectory at point $x \notin A \cup B$ at time $t$ is

$$Z^{-1} e^{-\beta V(x)} q(x)(1 - q(x)). \tag{3.25}$$

This means that the total probability that the trajectory be reactive at time $t$ is

$$Z_{AB} = Z^{-1} \int_{\Omega_{AB}} e^{-\beta V(x)} q(x)(1 - q(x)) \mathrm{d}x, \tag{3.26}$$

and the probability density to observe a reactive trajectory at point $x \notin A \cup B$ at time $t$ conditional on it being reactive at time $t$ is

$$\rho_{AB}(x) = Z_{AB}^{-1} Z^{-1} e^{-\beta V(x)} q(x)(1 - q(x)). \tag{3.27}$$

This expression was first derived in [52]. Furthermore, the probability current of reactive trajectories in (3.15) reduces to

$$J_{AB}(x) = Z^{-1}\beta^{-1} e^{-\beta V(x)} \Gamma^{-1} \nabla q(x) \tag{3.28}$$

and, consequently, the expressions for the rate in (3.17) and (3.19) take the form

$$k_{AB} = Z^{-1}\beta^{-1} \int_{\partial\mathcal{S}} \hat{n}_{\partial\mathcal{S}}(x) \cdot e^{-\beta V(x)} \Gamma^{-1} \nabla q(x) \mathrm{d}\sigma_{\partial\mathcal{S}}(x), \tag{3.29}$$

and

$$k_{AB} = Z^{-1}\beta^{-1} \int_{\Omega_{AB}} e^{-\beta V(x)} \nabla q(x)^T \cdot \Gamma^{-1} \nabla q(x) \mathrm{d}x, \tag{3.30}$$

respectively, where $\hat{n}_{\partial\mathcal{S}}(x)$ denotes the unit normal to the dividing surface $\partial\mathcal{S}$ pointing toward $B$ and $\mathrm{d}\sigma_S(x)$ is the surface element on $\partial\mathcal{S}$.

## 3.3. TPT in the Langevin Case

The results of TPT can be generalized to systems described by the Langevin equation introduced in Section 2.1.10:

$$\begin{aligned} \dot{x}_i(t) &= m_i^{-1} p_i(t), \\ \dot{p}_i(t) &= -\frac{\partial V(x(t))}{\partial x_i} - \gamma_i m_i^{-1} p_i(t) + \sqrt{2\gamma_i \beta^{-1}} \zeta_i(t), \end{aligned} \tag{3.31}$$

where $p = (p_1, p_2, \ldots, p_d) \in \mathbb{R}^d$ is the momentum of the particles, $m_i$ is the mass of $x_i$ and the other quantities are as in (3.22).

As mentioned earlier, the main difference is that the Langevin equation in (3.31) defines a non-reversible diffusion process on the phase space $(x, p)$ and the associated generator $\mathfrak{L}_{bw}$ is a degenerated partial differential operator.

Let $A \subset \mathbb{R}^{2d}$ be the reactant and $B \subset \mathbb{R}^{2d}$ be the product state in phase-space $(x, p)$. For the Langevin dynamics, the forward committor equation in (3.6) reduces to

$$\begin{cases} 0 = \mathfrak{L}_{bw} q \\ \quad = \beta^{-1}\Gamma : \nabla_p \nabla_p q + M^{-1} p \cdot \nabla_x q, \\ \qquad - \nabla_x V \cdot \nabla_p q - \Gamma M^{-1} p \cdot \nabla_p q & \text{in } \mathbb{R}^{2d} \setminus (A \cup B) \\ q = 0 & \text{on } \partial A, \\ q = 1 & \text{on } \partial B, \end{cases} \tag{3.32}$$

whereas the backward committor function $q_b(x, p)$ satisfies the backward committor equation

$$\begin{cases} 0 = \mathfrak{L}^R_{bw} q_b \\ \quad = \beta^{-1}\Gamma : \nabla_p \nabla_p q_b - M^{-1} p \cdot \nabla_x q_b \\ \qquad + \nabla_x V \cdot \nabla_p q_b - \Gamma M^{-1} p \cdot \nabla_p q_b & \text{in } \mathbb{R}^{2d} \setminus (A \cup B), \\ q_b = 1 & \text{on } \partial A, \\ q_b = 0 & \text{on } \partial B. \end{cases} \tag{3.33}$$

Notice that $q(x, p)$ can be related to $q_b(x, p)$ by

$$q_b(x, p) = 1 - q(x, -p), \tag{3.34}$$

provided that the sets $A$ and $B$ are point symmetric to each other with respect to the origin.

**Remark 3.3.1.** *The uniform ellipticity of the operator $\mathcal{L}_{bw}$ in the Smoluchowski case is essential for the existence a classical solution of the associated committor equation (cf.Theorem 2.1.4). Unfortunately, in case of the Langevin dynamics the backward operator $\mathcal{L}_{bw}$ is degenerate, but not elliptic (cf. Sect. 2.1.6) and up to our knowledge there does not exist any general theorem which states conditions for the existence of classical solutions of (3.32) and (3.33). Nevertheless, our numerical investigations on the committor equations in the Langevin case (as presented in Sect. 3.9) will show that at least for low-dimensional simple domains $\Omega \subset \mathbb{R}^2$ and reasonable parameters there exist sufficiently smooth solutions of (3.32) and (3.33).*

In terms of these quantities, the probability density to observe a reactive trajectory at $(x, p)$ at time $t$ conditional on the trajectory being reactive at time $t$ now becomes (cf. (3.27))

$$\rho_{AB}(x, p) = Z_{AB}^{-1} Z^{-1} e^{-\beta H(x,p)} q(x, p) q_b(x, p), \tag{3.35}$$

where $H(x, p) = V(x) + \frac{1}{2} p^T M^{-1} p$ is the Hamiltonian, $Z = \int_{\mathbb{R}^d \times \mathbb{R}^d} e^{-\beta H(x,p)} \mathrm{d}x\mathrm{d}p$ is the partition function and $Z_{AB}$ is the total probability that the trajectory be reactive at time $t$ (cf. (3.26)):

$$Z_{AB} = Z^{-1} \int_{\Omega_{AB}} e^{-\beta H(x,p)} q(x, p) q_b(x, p) \mathrm{d}x\mathrm{d}p, \tag{3.36}$$

where $\Omega_{AB} = \mathbb{R}^{2d} \setminus (A \cup B)$. The probability current of the reactive trajectories can be obtained as well (cf. (3.28)):

$$J_{AB}(x,p) = Z^{-1} e^{-\beta H(x,p)} \big( J^x_{AB}(x,p), J^p_{AB}(x,p) \big), \tag{3.37}$$

where $J^x_{AB}(x,p)$ and $J^p_{AB}(x,p)$ are the components of the current in the directions of $x$ and $p$, respectively, and given by

$$\begin{aligned} J^x_{AB}(x,p) =& q(x,p) q_b(x,p) p, \\ J^p_{AB}(x,p) =& - q(x,p) q_b(x,p) \nabla V(x) \\ & + \beta^{-1} q_b(x,p) \Gamma \nabla_p q(x,p) - \beta^{-1} q(x,p) \Gamma \nabla_p q_b(x,p). \end{aligned}$$

Out of the current the reaction rate can be computed (cf. (3.29))

$$k_{AB} = \int_{\partial \mathcal{S}} \hat{n}_{\partial \mathcal{S}}(x,p) \cdot J_{AB}(x,p) \mathrm{d}\sigma_{\partial \mathcal{S}}(x,p), \tag{3.38}$$

where $\partial \mathcal{S}$ is any dividing surface in phase-space between $A$ and $B$, $\hat{n}_{\mathcal{S}}(x,p)$ is the unit normal on $\partial \mathcal{S}$ pointing toward $B$ and $\mathrm{d}\sigma_{\mathcal{S}}(x,p)$ is the surface element on $\partial \mathcal{S}$. (3.38) can be re-expressed via (3.19) as a volume integral as (cf. (3.30))

$$\begin{aligned} k_{AB} = Z^{-1} \beta^{-1} \int_{\Omega_{AB}} & \nabla_p q(x,p)^T \cdot \Gamma \nabla_p q(x,p) \\ & \times e^{-\beta H(x,p)} \mathrm{d}x \, \mathrm{d}p. \end{aligned} \tag{3.39}$$

The streamlines of the probability current of reactive trajectories can also be defined as the ensemble of solutions of (cf. (3.20))

$$\begin{cases} \dfrac{dx(\tau)}{d\tau} = J^x_{AB}(x(\tau), p(\tau)), \\ \dfrac{dp(\tau)}{d\tau} = J^p_{AB}(x(\tau), p(\tau)), \end{cases} \tag{3.40}$$

and they can be used to define reaction tubes carrying a given percentage of the probability flux of reactive trajectories as in the overdamped case.

The only additional difficulty with (3.32) absent with (3.24) is that, because the differential operator in (3.32) is degenerate (i.e. hypo-elliptic but not elliptic), in order to be able to impose the Dirichlet boundary conditions on $\partial A$ and $\partial B$, the unit normal to these sets at $(x,p)$ must span the velocity degrees of freedom everywhere except maybe on a set of zero measure on $\partial A$ and $\partial B$. How to solve (3.32) in the context of the simple example considered in Section 3.9, is discussed in Section A.1 in the Appendix.

## 3.4. Numerical Aspects

Here we briefly discuss how we performed the numerics on the examples discussed below. In order to get an accurate approximation of the committor functions $q(x)$ and $q(x,p)$, we derived a stable finite differences scheme for the discretization of (3.24) and (3.32) and implemented the resulting scheme in MATLAB. In all numerical computations involving (3.24) we choose a rectangular domain $\Omega \subset \mathbb{R}^2$ and a uniform

mesh. The Dirichlet conditions for $q(x)$ are included into our scheme by defining discrete sets $A$ and $B$ via the mesh. For the details of the respective finite difference schemes and the proofs of stability and convergence see Section A.1 in the Appendix.

**Remark 3.4.1.** *We want to emphasize here that our extensive numerical experiments have shown that the results which will be presented in the next sections are stable under refinement of the underlying discretization meshes.*

To compare and test the predictions of TPT, we also computed some of the statistical quantities provided by TPT by means of direct numerical simulation (DNS) of the dynamical equations (3.22) and (3.31). As explained earlier, an ensemble of reactive trajectories can be computed by pruning a sufficiently long trajectory. This was done by discretizing (3.22) and (3.31) in such a way that long-term stability is achieved. The results presented below are based on the Euler-Maruyama-scheme for the Smoluchowski dynamics and an appropriate second order scheme for the Langevin dynamics [93] which both have been used with sufficiently small discretization time steps to guarantee stability. From the long trajectory generated by DNS, the approximation of the probability density function of reactive trajectories was obtained by binning the region between the reactant and product state and computing the ratio between the time spent by the reactive trajectories in each bin and the total time the long trajectory was reactive. The reaction rate was obtained by counting the number $N$ of transitions from $A$ to $B$ in the long trajectory of length $T$, and dividing this number by $T$. It should be stressed that the trajectory must be extremely long in order to obtain a statistically accurate estimate of $q(x)$, $q(x,p)$ and $k_{AB}$ by DNS, which makes the DNS much more expensive than the numerical solution of (3.24) and (3.32).

## 3.5. Diffusion in the Double-Well Potential

For our first example, we choose the two-dimensional potential (here and below we denote $(x,y) = (x_1, x_2)$):

$$V(x,y) = \tfrac{5}{2}(x^2-1)^2 + 5y^2 \tag{3.41}$$

which is a combination of a double well potential in $x$-direction and a harmonic potential in $y$-direction. The local minima at $(-1,0)$ and $(0,1)$ are separated by a saddle point at $(0,0)$. We choose the inverse temperature $\beta = 1$ such that the process spends most of its time within the two wells, and we also set $\gamma_x = \gamma_y = 1$. The equilibrium distribution of the Smoluchowski dynamics (3.22) associated with (3.41) is depicted in Figure 3.2.

For the reactant and product states, $A$ and $B$, we choose the two neighborhoods of the two minima of the potential at $(-1,0)$ and $(1,0)$ such that they include all states $x$ that satisfy $V(x,y) < 0.4$; as in all subsequent computations these sets are replaced by the sets of all mesh points satisfying this condition. We also restricted the computation to the domain $\Omega = [-1.5, 1.5] \times [-1, 1]$, which is large enough so that the potential is high at the boundaries (and hence the Boltzmann-Gibbs probability density is very small there). To discretize $\Omega$, we used a uniform mesh of consisting of $500 \times 500$ mesh points.

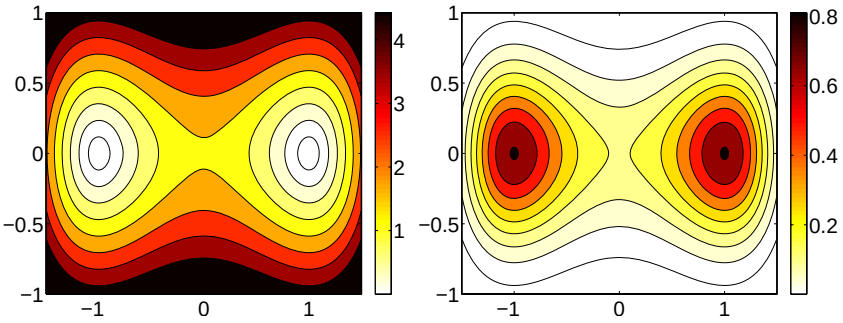


Figure 3.2.: Left: Contour plot of the double-well potential. Right: Contour plot of the Boltzmann-Gibbs probability density function $Z^{-1}e^{-\beta V(x,y)}$. Results for $\beta = 1$. The regions around the minima at $(-1, 0)$ and $(1, 0)$ contain most of the probability, i.e. they are metastable.

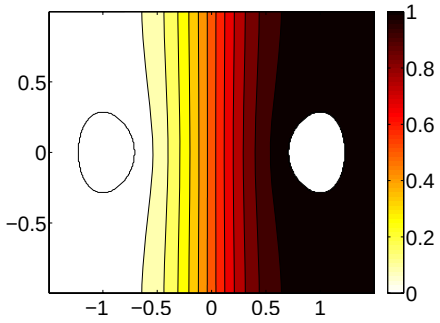


Figure 3.3.: Contour plot of the committor function solution $q(x, y)$ of (3.24) at inverse temperature $\beta = 1$. The white regions are the reactant state $A$ and product state $B$ ($A$ is the left, $B$ at the right). The level sets (isolines) of $q(x, y)$ are the regions from which the probability to reach first $A$ rather $B$ is uniform.

### 3.5.1. Committor Function

Figure 3.3 shows the level sets (isolines) of the committor function $q(x, y)$ obtained by solving (3.24) for this example. The left-right symmetry of the level sets of $q(x, y)$ with respect to the piece of the vertical axis $S = \{(0, y)| - 1 \leq y \leq 1\}$ which includes the saddle point $(0, 0)$ is a consequence of the choice of domain $\Omega$, the symmetry of the potential (3.41) and the symmetry between $A$ and $B$. In particular, it is clear that the probability to reach $A$ before $B$ should be $\frac{1}{2}$ for all points on $S$, i.e. $q(0, y) = \frac{1}{2}$ for all $-1 \leq y \leq 1$. This prediction is confirmed by the numerics.

### 3.5.2. Probability Density Function of Reactive Trajectories

Knowing $q(x, y)$ we can compute the probability density function of reactive trajectories $\rho_{AB}(x, y)$ via (3.27). This probability density function is shown in Figure 3.4. The density $\rho_{AB}(x, y)$ is peaked around the saddle point $(0, 0)$ which indicates that the region around the saddle point is the dynamical bottleneck (transition state region) for the reaction.

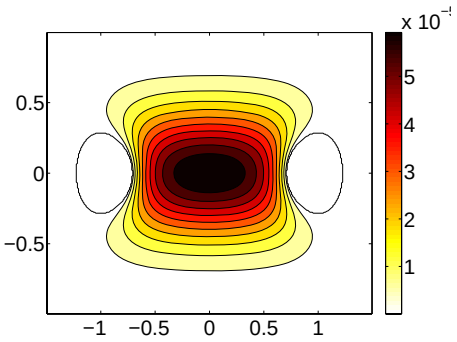


Figure 3.4.: Contour plot of the probability density function $\rho_{AB}(x, y)$ of reactive trajectories obtained via (3.27). Results for $\beta = 1$.

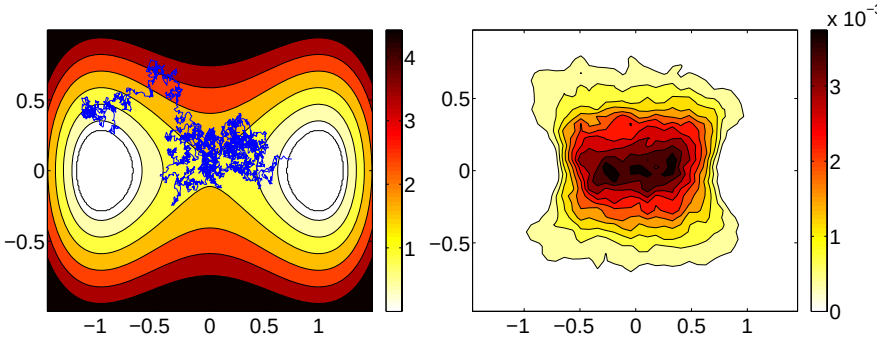


Figure 3.5.: Left: A typical reactive trajectory. Right: Probability density function of reactive trajectories computed via DNS based on 300 reactive trajectories and represented on a $40 \times 40$ box-discretization of the domain $\Omega$. Results for $\beta = 1$.

For comparison, the probability density function of reactive trajectories $\rho_{AB}(x, y)$ was also computed by DNS. In the left panel of Figure 3.5 a typical reactive trajectory is shown.

In the right panel of Figure 3.5 the probability density function of reactive trajectories as computed via DNS is shown. The result of DNS agrees with the prediction of TPT shown in Figure 3.4. Notice however that the probability density $\rho_{AB}(x, y)$ obtained by DNS is subject to significantly larger errors of statistical origin.

### 3.5.3. Probability Current of Reactive Trajectories and its Streamlines

Knowing $q(x, y)$, we can also compute the probability current of reactive trajectories via (3.28) and its streamlines via (3.20). These streamlines are shown in the right panel of Figure 3.6.

In order to better visualize the probability current as well as the reaction tubes mentioned in Section 3.1, we did the following: First we computed the intensity of the probability current on a dividing surface of interest, for which we choose the isocommittor $\frac{1}{2}$ surface, $S_{1/2} = \{(x, y) : q(x, y) = \frac{1}{2}\}$. Since the isocommittor surface $S_{1/2}$ is simply the piece of the $y$-axis in $\Omega$, the intensity $J_{AB} \cdot \hat{n}_{S_{1/2}}$ of the probability current on $S_{1/2}$ can be expressed by

$$J_{AB,1}(0, y) \cdot \hat{n}_{S_{1/2}} = \beta^{-1} Z^{-1} e^{-\beta V(0,y)} \frac{\partial q(0, y)}{\partial x}. \tag{3.42}$$

This intensity on $S_{1/2}$ is shown in the left panel of Figure 3.6. We observe that the intensity of the current is maximum at $(0, y) = (0, 0)$ which corresponds to the saddle point. This means that most reactive trajectories cross $S_{1/2}$ near the saddle point or, equivalently, that the probability flux of reactive trajectories across $S_{1/2}$ is concentrated near the saddle point.

Next, from each point $(0, y)$ on $S_{1/2}$ we transported the value of the current intensity $J_{AB}(0, y) \cdot \hat{n}_{S_{1/2}}$ backwards and forwards along each streamline of the current $J_{AB}(x, y)$ until it enters the states $A$ and $B$. With this procedure, we give each point along a streamline the value of the current intensity evaluated at the point on $S_{1/2}$ through which the streamline goes. This is how the coloring in the right panel of Figure 3.6 was obtained: the darker the region, the higher the current intensity is. Regions in this figure which include all the greys down to a certain level form reactions tubes carrying a given percentage of the probability flux of reactive trajectories (the lower the level of grey, the higher the percentage; in this example, the tube in black already carries 42% of the flux).

### 3.5.4. Reaction Rate

Now we turn our attention to the reaction rate $k_{AB}$. Choosing $S_{1/2}$ as dividing surface in (3.29), this expression for the reaction rate reduces to

$$k_{AB} = \beta^{-1} Z^{-1} \int_{-1}^{1} e^{-\beta V(0,y)} \frac{\partial q(0, y)}{\partial x} dy. \tag{3.43}$$

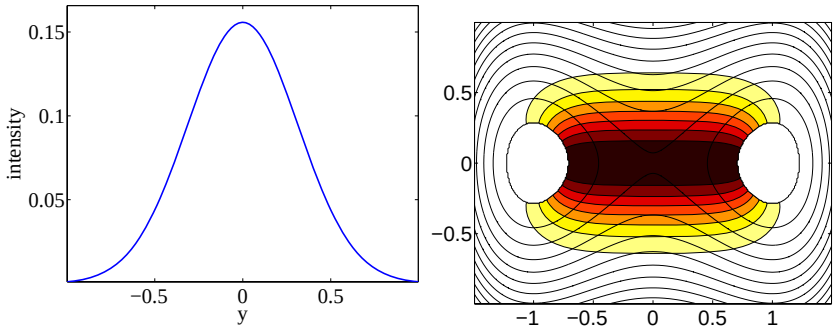


Figure 3.6.: Left: Intensity 3.42 of the probability current of reactive trajectories on the isocommittor surface $S_{1/2} = \{(x, y) : q(x, y) = 0.5\} = \{(0, y) : -1 \leq y \leq 1\}$. Right: Streamlines of the probability current $J_{AB}(x, y)$ colored according to the intensity of the current on the isocommittor surface $S_{1/2}$. Results for $\beta = 1$. The darker the color, the higher the intensity of the probability current of reactive trajectories through this region.

| | |
|---|---|
| $k_{AB}$ via (3.43) | $1.225 \cdot 10^{-1}$ |
| $k_{AB}$ via (3.44) | $1.226 \cdot 10^{-1}$ |
| $k_{AB}$ via DNS | $(1.230 \pm 0.029) \cdot 10^{-1}$ |

Table 3.1.: Reaction rate computed for the double-well potential for $\beta = 1$. The rate predicted by TPT is consistent with the rate computed via DNS (out of $N = 10^5$ reactive trajectories). The error given on the rate computed via DNS is the estimated statistical error. There is an additional error (not given) on all rates due to discretization of the domain; this error can be estimated from the difference between the rates obtained via (3.43) and via (3.44).

Alternatively, we can compute $k_{AB}$ via (3.30):

$$k_{AB} = \beta^{-1} Z^{-1} \int_{\Omega_{AB}} \left( \left( \frac{\partial q(x,y)}{\partial x} \right)^2 + \left( \frac{\partial q(x,y)}{\partial y} \right)^2 \right) \times e^{-\beta V(x,y)} \mathrm{d}x\mathrm{d}y. \tag{3.44}$$

We approximate the partial derivatives $\partial q/\partial x$ and $\partial q/\partial y$ which are involved in both expressions for the rate on the mesh used to compute the committor function.

We compare the rate $k_{AB}$ computed via DNS with the rates obtained from (3.43) and (3.44). Table 3.1 shows that the agreement of all different results is very good.

## 3.6. Entropic Barriers: Pure Diffusion

In our next example we consider pure diffusion in a square $\Omega = [0, 1] \times [0, 1]$ with two obstacles such that the domain becomes the $S$-shaped region shown in Figure 3.7. By pure diffusion we mean that we consider the Smoluchowski dynamics in a flat potential, $V(x, y) = 0$ in (3.22), except for the presence of hard walls at the boundary of the domain. We are interested in the statistics of the reactive trajectories starting

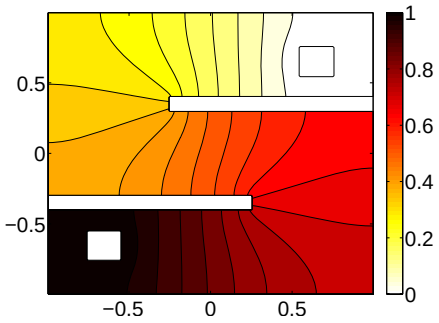


Figure 3.7.: Contour plot of the committor function $q(x, y)$ for the pure diffusion in the $S$-shaped domain. The reactant state $A$ and product state $B$ are the two squares in the upper-right and bottom-left corners, respectively. The two thin white rectangular regions connected to the vertical sides of the domain are hard walls. Results for $\beta = 1$. In this example, the Boltzmann-Gibbs probability density $Z^{-1}e^{-\beta V(x,y)}$ is uniform in the domain since $V(x, y) = 0$ except at the walls where it is infinity.

in a region near the upper-right corner (set $A$) and ending in a region near the bottom-left corner (set $B$), see Figure 3.7. In contrast with the previous example where the transition between $A$ and $B$ is constrained by a potential barrier, here the dynamics has to overcome an *entropic barrier*: it has to find its way between the two obstacles. Suppose we start the dynamics in $A$. The closer the dynamics gets to the region enclosed by the obstacles the higher the probability that the dynamics will finally reach the left-down corner before returning to $A$ because the probability to end up in $B$ depends only on the distance between the current position and the set $B$. Figure 3.7 shows the committor function $q(x, y)$ as computed for this example; its isolines nicely illustrate the particular behavior of the dynamics. From the symmetry of the domain $\Omega\backslash(A\cup B)$ it is clear that the isocommittor $\frac{1}{2}$ surface goes through the point $(0, 0)$. Therefore it is very likely to encounter a reactive trajectory between the obstacles, in the vicinity of isocommittor $\frac{1}{2}$ surface. In the left panel of Figure 3.8 we depict a typical reactive trajectory. One can see that the reactive trajectory spends most of its time between the obstacles. This is also obvious from the contour plot of the probability density function of reactive trajectories $\rho_{AB}(x, y)$ shown in the right hand panel of Figure 3.8. Notice how complicated the reactive trajectory is in this example and how much simpler $\rho_{AB}(x, y)$ is. The probability current of reactive trajectories (not shown) can also be computed in this example but it turns out to be very simple (basically, the streamlines follow the $S$-shape). In order to complete our observation for this example, Table 3.2 gives the values of the transition rates computed via TPT and via DNS. Again the values agree within numerical accuracy.

This example clearly shows that TPT is not restricted to situations in which the reaction pathway is determined by energy effects, as in the example in Section 3.5, but it also allows one to handle situations where entropic effects dominate.

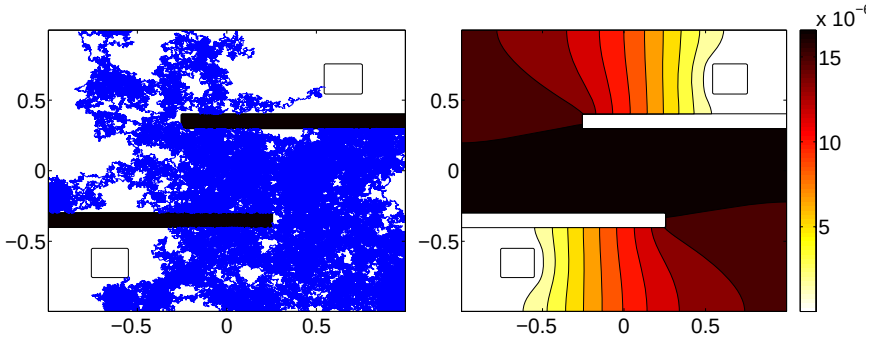


Figure 3.8.: Left: A typical reactive trajectory. Right: Contour plot of the probability density function of reactive trajectories $\rho_{AB}(x, y)$. Results for $\beta = 1$.

| | |
|---|---|
| rate via (3.29) | $4.455 \cdot 10^{-2}$ |
| rate via (3.30) | $4.443 \cdot 10^{-2}$ |
| rate via DNS | $(4.425 \pm 0.144) \cdot 10^{-2}$ |

Table 3.2.: The reaction rate $k_{AB}$ for the pure diffusion in the $S$-shaped domain. Results for $\beta = 1$ and $N = 10^5$ in the DNS.

## 3.7. Entropic Switching

### 3.7.1. Diffusion in a Three-Hole Potential

In the next example, we study an example with two different reaction channels. For this purpose, we choose the three-hole potential

$$\begin{aligned} V(x,y) =& 3e^{-x^2-(y-\frac{1}{3})^2} - 3e^{-x^2-(y-\frac{5}{3})^2} \\ & - 5e^{-(x-1)^2-y^2} - 5e^{-(x+1)^2-y^2} \\ & + 0.2x^4 + 0.2(y-\tfrac{1}{3})^4 \end{aligned} \tag{3.45}$$

which has already been considered in [73, 25].

As one can see in the left panel of Figure 3.9 the potential (3.45) has two deep minima approximately at $(\pm 1, 0)$, a shallow minimum approximately at $(0, 1.5)$,

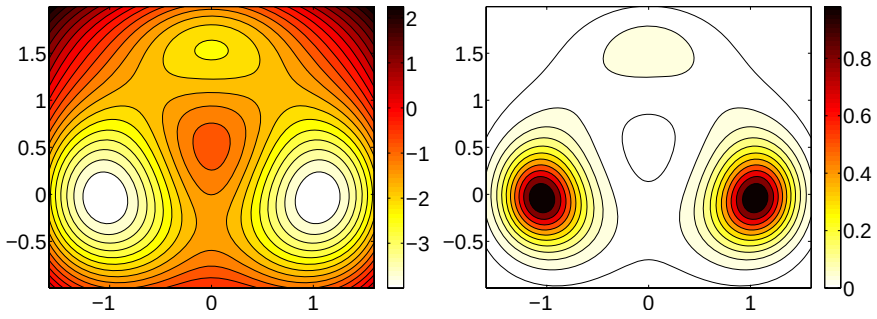


Figure 3.9.: Left: Contour plot of the three-hole potential. Right: Contour plot of the Boltzmann-Gibbs probability density function $Z^{-1}e^{-\beta V(x,y)}$ at $\beta = 1.67$.

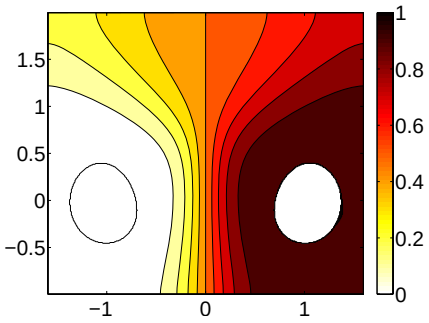


Figure 3.10.: Contour plot of the committor function $q(x, y)$ at $\beta = 1.67$. The isolines of the committor function are spread in the upper region of the potential because reactive trajectories get trapped in the upper shallow minima. The symmetry of the domain and the sets $A$ and $B$ implies that the isocommittor surface $\frac{1}{2}$ is $S_{1/2} = \{(0, y) : -2 \leq y \leq 2\}$. Results for a $350 \times 350$ mesh discretization.

three saddle points approximately at $(\pm 0.6, 1.1)$, $(-1.4, 0)$ and a maximum at $(0, 0.5)$. Thus, the two deep minima are connected by an upper and a lower channel, and the upper channel contains the additional, less-pronounced minimum. The dynamical bottlenecks in the upper channel are the two saddle points with equal potential energy whereas the dynamics in the lower channel has only to overcome one saddle point whose potential energy is higher compared to the other two. It is known from large deviation theory [38] that in the limit $\beta \to \infty$ the reaction will occur via the upper channel with probability 1 since the energy barrier is lower there. Therefore we expect that the dynamics prefers the upper channel at low (finite) temperature. At higher temperature, however, the lower channel should be preferred (since it is direct). This entropic switching effect was first discovered and analyzed in [73]. There the authors used the gradient of the mean first passage time (MFPT) (cf. Remark 3.1.2) with respect to a given state to detect the transition channels and their dependence on the temperature.

In this example, we performed experiments at two inverse temperature $\beta = 6.67$ (low temperature), which is such that the upper channel is the preferred reaction tube, and $\beta = 1.67$ (high temperature), which is such that the lower channel is the preferred reaction tube.

In Figure 3.10 we show the contour plot of the committor function at $\beta = 1.67$. As in the previous examples the symmetry of the domain $\Omega_{AB}$ explains that the isocommittor surface $\frac{1}{2}$ is $S_{1/2} = \{(0, y) : -2 \leq y \leq 2\}$. Notice how the presence of the shallow minima in the upper channel spreads the level sets of $q(x, y)$ in this region. This follows from the fact that the reactive trajectories going through the upper channel get trapped in the shallow well for a long period of time before exiting towards the set $B$. Notice that it also implies that the isocommittor $\frac{1}{2}$ surface goes through the shallow minima and not through one of the two upper saddle points. The committor function at $\beta = 6.67$ (not shown) is very similar to the one at $\beta = 1.67$ (though, as we will see below, the probability density function and the probability current of reactive trajectories are very different). The left panel of Figure 3.11 reveals the similarity between the (forward) committor function and the eigenvector

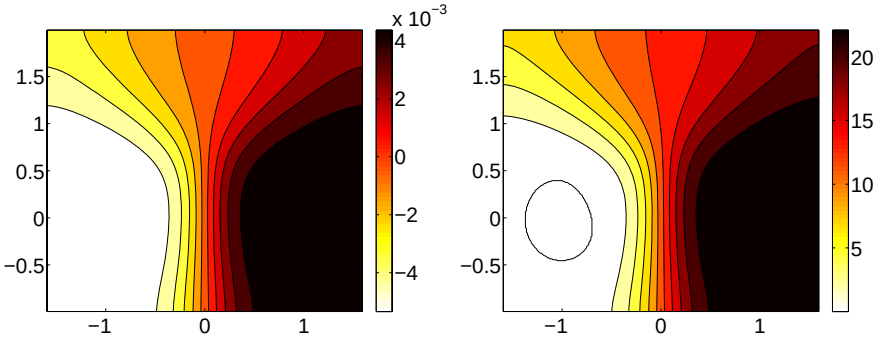


Figure 3.11.: Left: Contour plot of the eigenvector associated with the first non-trivial right eigenvalue of the discretization matrix $\overline{D}_h$ resulting from the finite differences discretization of the generator $\mathcal{L}_{bw}$ on the entire domain $\Omega$ together with Neumann boundary condition. Right: Contour plot of the MFPT with respect to the set $A$ as also analyzed in [73]. Results for $\beta = 1.67$ and a $350 \times 350$ mesh discretization.

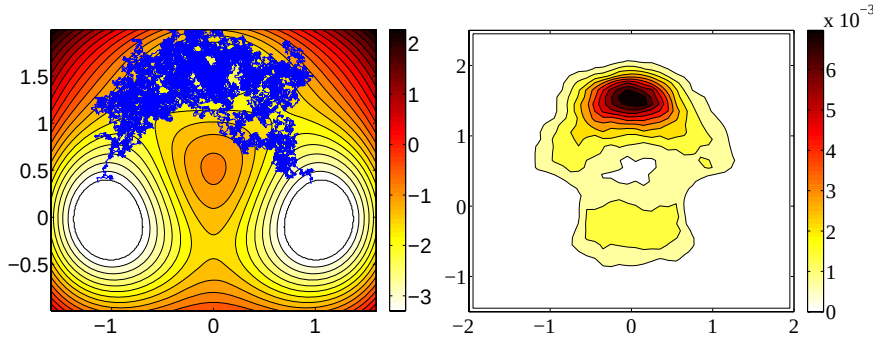


Figure 3.12.: Left: A typical reactive trajectory at a high temperature $\beta = 1.67$ taking the upper channel with the two saddle points with lowest energy. Right: Contour plot of the probability density function of reactive trajectories computed via DNS at $\beta = 1.67$ from 500 reactive trajectories using a $40 \times 40$ box-discretization of the domain $\Omega = [-2, 2] \times [-1.5, 1.5]$.

associated with the first non-trivial right eigenvalue of the discretization matrix $\overline{D}_h$ resulting from the finite differences discretization of the generator $\mathcal{L}_{bw}$ on the domain $\Omega_{AB}$. Furthermore, the right panel of Figure 3.11 illustrates the similarity between the forward committor function and the MFPT with respect to the set $A$ which is a specialty of this example and will not be guaranteed in general.

Now we turn our attention to the probability density function of reactive trajectories $\rho_{AB}(x, y)$ for this example. The panels in Figure 3.12 illustrate this situation for $\beta = 1.67$ (high temperature) as computed via DNS. In Figure 3.13 we depict the probability density function of reactive trajectories from TPT computed at two different temperatures. The left panel shows the density for a low temperature ($\beta = 6.67$) and the lower one for a high temperature ($\beta = 1.67$). The first observation is that both densities attain their maximum in the shallow minima. This is because the shallow minima catches the dynamics on its way from $A$ to $B$. As a consequence, the reactive trajectories spend a long time within this region and

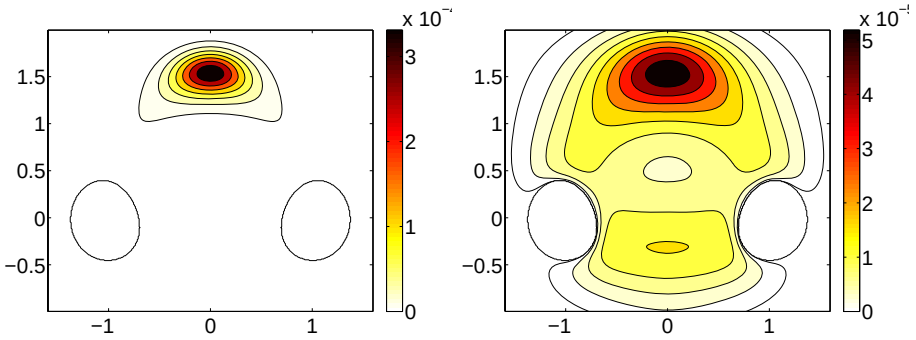


Figure 3.13.: Contour plots of the density $\rho_{AB}(x, y)$ for two different temperatures. Left: low temperature $\beta = 6.67$; Right: high temperature $\beta = 1.67$. In both cases $\rho_{AB}(x, y)$ attains its maximum in the shallow minima.

| | $\beta = 6.67$ | $\beta = 1.67$ |
|---|---|---|
| rate via (3.29) | $9.47 \cdot 10^{-8}$ | $1.912 \cdot 10^{-2}$ |
| rate via (3.30) | $9.22 \cdot 10^{-8}$ | $1.924 \cdot 10^{-2}$ |
| rate via DNS | | $(1.918 \pm 0.052) \cdot 10^{-2}$ |

Table 3.3.: Reaction rates for the three-hole potential for $\beta = 6.67$ and $\beta = 1.67$. One can see that for $\beta = 1.67$ the rate computed via DNS ($N = 10^5$) is consistent with those predicted from TPT. For $\beta = 6.67$ the rate is so small that any computation via DNS would lead to totally unreasonable effort (to obtain $N = 10^5$ reactive trajectories, it would require to generate a long trajectory of length $T \approx 10^5/k_{AB} = 10^{12}$). The computations via finite difference discretization of (3.24) take only a few seconds on a standard PC.

therefore the probability to encounter a reactive trajectory there increases. However, one can see that at the high temperature that there is a certain probability to encounter a reactive trajectory in the lower channel. But which reaction channel does the dynamics prefer depending on the temperature? From the viewpoint of the density $\rho_{AB}(x, y)$ we cannot answer this question since the long residency of reactive trajectories in the vicinity of the shallow minima spoils the information about the relative *number* of reactive trajectories going there.

To answer the question of which reaction channel is preferred at different temperatures we must consider the probability current of reactive trajectories $J_{AB}(x, y)$. In Figure 3.14 we show the transition tubes computed via its streamlines with colors induced by the intensity of the probability current on the isocommittor surface $\frac{1}{2}$, using the procedure explained in Section 3.5.3. One can clearly see that the transition tubes give the desired information. At the low temperature (left panel) the preferred transition channel is the upper one and at the high temperature (right panel) it is the lower one. This result is consistent with observations made in [73]. We complete this example by stating the reaction rate for the two temperatures in Table 3.3. As in the previous examples we choose the isocommittor surface $\frac{1}{2}$ for the rate computations via (3.43).

This example shows that TPT is able to handle situations with multiple reaction

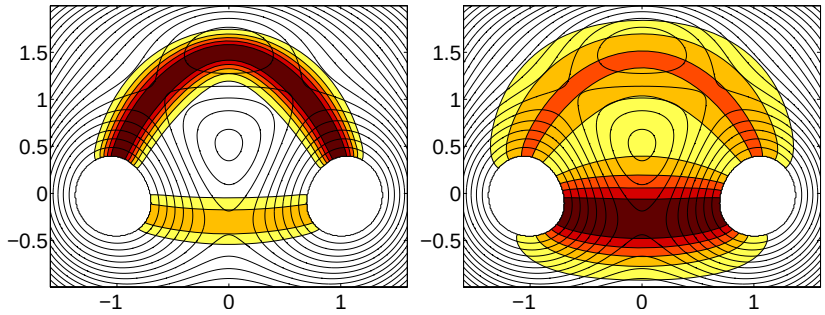


Figure 3.14.: Streamlines of the probability current of reactive trajectories colored according to the intensities of the probability current on the isocommittor $\frac{1}{2}$ surface for two different temperatures. Left: At the low temperature $\beta = 6.67$ the upper channel is the preferred reaction channel. Right: At the high temperature $\beta = 1.67$ most of the reactive trajectories take the lower channel.

channels, possibly with intermediate metastable states along them, and can distinguish which channel is preferred depending on the temperature (entropic switching). It also shows that all the objects provided by TPT – the probability density of the reactive trajectories, their probability current and the associated streamlines – are necessary (and sufficient) to understand the mechanism of the reaction, while $\rho_{AB}(x, y)$ alone is not.

### 3.7.2. Diffusion in a Rough Three-Hole Potential

In this section we are interested in the ensemble of reactive trajectories and its statistical properties for a Smoluchowski process in a *rough* potential landscape. To make things comparable, we perturbed the three-hole potential from the previous section by adding a periodic function with randomly drawn coefficients. To be more precise, we consider the potential

$$\tilde{V}(x, y) = V(x, y) + \sum_{k,l=1}^{n} \left[ c_{kl} \cos(2\pi(kx + ly)) + d_{kl} \sin(2\pi(kx - ly)) \right], \qquad (3.46)$$

where $V(x, y)$ is the three-hole potential in (3.45) and the real coefficients $c_{kl}, d_{kl}, 1 \leq k, l \leq n$ are drawn from a normal distribution $\mathcal{N}(0, \delta^2)$ with variance $\delta^2$. For our numerical experiments, we chose $n = 5$ and $\delta = 0.05$. As one can see in Figure 3.15 the perturbed potential still exhibits three regions of attraction separated by a multitude of small barriers.

The guiding question is whether the entropic switching behavior is conserved despite the perturbation and, in particular, in which way the transition channels deviate from those resulting in a smooth potential (cf. Fig. 3.14). As the sets $A$ and $B$, we chose the same sets as in the smooth three-hole potential example. The first row in Figure 3.16 shows the (forward) committor function at low temperature $\beta = 6.67$ (left upper panel) and at high temperature $\beta = 6.67$ (right upper panel). As expected, the lower the temperature the bigger the impact of the roughness of the potential landscape on the committor function because at low temperature the

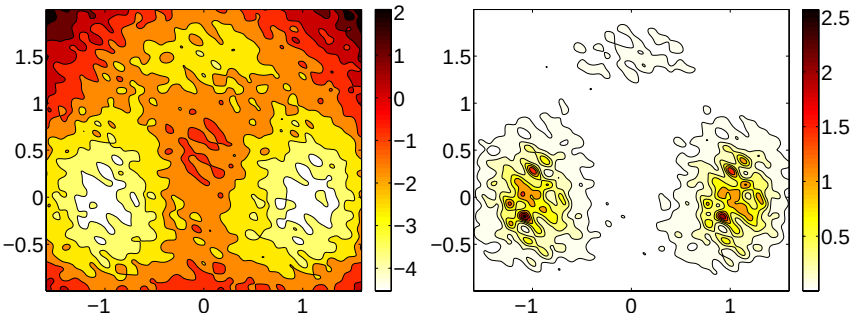


Figure 3.15.: Left: Contour plot of the perturbed three-hole potential in (3.46). Right: Contour plot of the associated Gibbs probability density function $Z^{-1}e^{-\beta\tilde{V}(x,y)}$ at $\beta = 1.67$. Results for the perturbation parameters $n = 5$ and $\delta = 0.05$.

| $\delta^2$ | 0.01 | 0.05 | 0.1 | 0.2 | 0.5 |
|---|---|---|---|---|---|
| $k_{AB}$ | $1.91 \cdot 10^{-2}$ | $1.79 \cdot 10^{-2}$ | $1.08 \cdot 10^{-2}$ | $4.45 \cdot 10^{-3}$ | $2.42 \cdot 10^{-5}$ |

Table 3.4.: The transition rate $k_{AB}$ computed via (3.30) as a function of the variance $\delta^2$. Results for $\beta = 1.67$ and $n = 5$.

dynamics gets trapped in any local minima. Notice that even for the perturbed potential, the geometry of the level sets of the eigenvector associated with the first non-trivial right eigenvalue of the discretization matrix[1] $\overline{D}_h$ (shown in the second row of Figure 3.16) is very similar to the geometry of the level sets of the corresponding committor function, respectively.

We have seen that in the smooth three-hole potential example in Section 3.7.1, the distribution $\rho_{AB}$ of reactive trajectories does not allow to make any prediction about the preferred reaction channel. As one can see in the panels of Figure 3.17, in the case of a rough potential landscape the distribution $\rho_{AB}$ does not even give an idea of a single reaction channel. However, as illustrated in the panels of Figure 3.18, the streamlines of the probability current of reactive trajectories reveal the reaction channels and, furthermore, show that despite the perturbation of the landscape the global transition behavior is comparable to the transition behavior in the smooth potential landscape.

We end this example by stating in Table 3.4 the transition rate $k_{AB}$ (computed via (3.30)) as a function of the variance $\delta^2$ of the normal distribution $\mathcal{N}(0, \delta^2)$. The decrease of the transition rate as $\delta^2$ increases can be explained by noting that in a rough potential landscape the dynamics gets trapped in each local minima and, thus, as the roughness increases it becomes more difficult for the dynamics to make a transition from $A$ to $B$.

[1] $\overline{D}_h$ is meant to be the matrix which results from the finite difference discretization of the operator $\mathcal{L}_{bw}$ on the *entire* domain $\Omega$ under incorporation of the Neumann boundary conditions.

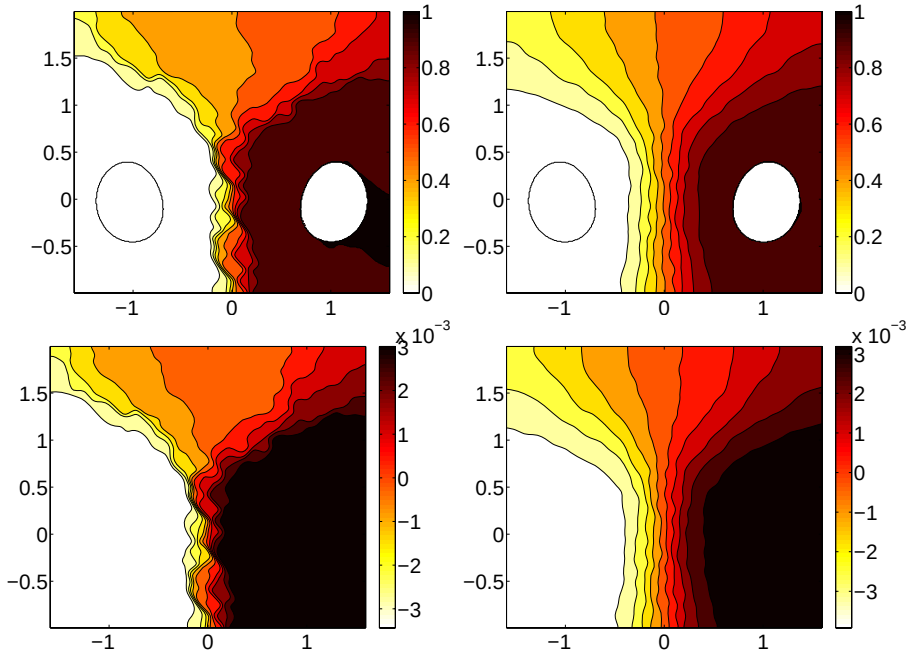


Figure 3.16.: Contour plot of the committor function $q(x, y)$ at low temperature $\beta = 6.67$ (upper left panel) and at high temperature $\beta = 1.67$ (upper right). The second row shows the contour plot of the eigenvector associated with the first non-trivial right eigenvalue of the discretization matrix $\overline{D}_h$: left lower panel at $\beta = 6.67$ and right lower panel at $\beta = 1.67$. Obviously, the geometry of the level sets of the eigenvector and the level sets of the committor function is very similar, respectively.

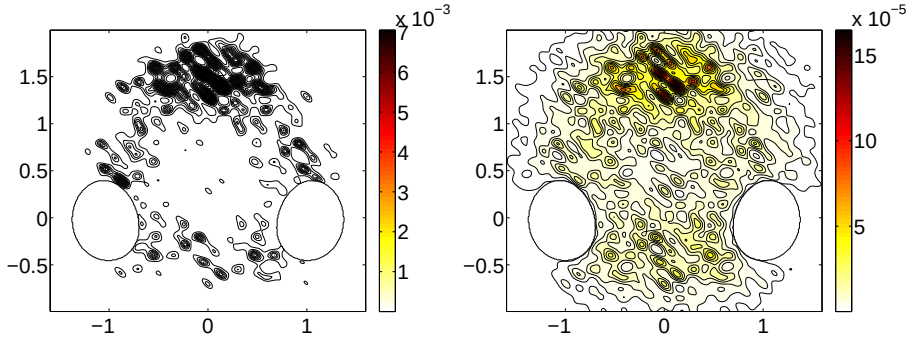


Figure 3.17.: In this figure we illustrate the probability density function $\rho_{AB}(x, y)$ of the reactive trajectories in the perturbed three-hole potential for two different temperatures. Left: low temperature $\beta = 6.67$; Right: high temperature $\beta = 1.67$.

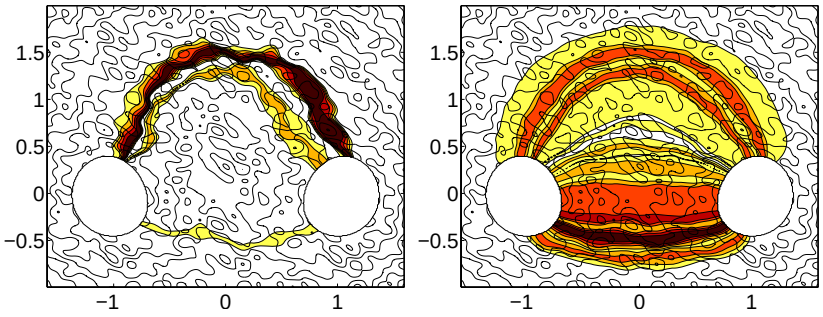


Figure 3.18.: Streamlines of the probability current of reactive trajectories in the perturbed three-hole potential colored according to the intensities of the probability current on the isocommittor $\frac{1}{2}$ surface for two different temperatures. Left: Despite the perturbation, at the low temperature $\beta = 6.67$ the upper channel is the preferred reaction channel whereas at the high temperature $\beta = 1.67$ (right panel) most of the reactive trajectories still take the lower channel.

## 3.8. Different Time-Scales: Fast-Slow Diffusion in a Double-Well Potential

In the last example for the Smoluchowski dynamics we consider a diffusion process with two variables subject to different friction coefficients leading to two different time scales. For this purpose we consider a process generated by

$$\begin{aligned} \dot{x}(t) &= -\frac{\partial V(x(t), y(t))}{\partial x} + \sqrt{2\beta^{-1}}\,\eta_x(t) \\ \epsilon\dot{y}(t) &= -\frac{\partial V(x(t), y(t))}{\partial y} + \sqrt{2\beta^{-1}\epsilon}\,\eta_y(t). \end{aligned} \tag{3.47}$$

This system is a special case of (3.22) with $\gamma_x = 1$ and $\gamma_y \equiv \epsilon > 0$. For $\epsilon \ll 1$, the variable $y$ is fast compared to $x$. For details see [83]. Despite the different time scales, the equilibrium distribution still is given by the Boltzmann-Gibbs density $Z^{-1}e^{-\beta V(x,y)}$ for every value of $\epsilon > 0$. For the potential $V$, we choose a double-well potential in $y$-direction which is coupled to a harmonic potential in $x$-direction

$$V(x, y) = 5(y^2 - 1)^2 + 1.25(y - \tfrac{1}{2}x)^2. \tag{3.48}$$

The potential attains two local minima at $(-2, -1)$ and $(2, 1)$ which are separated by a saddle point at $(0, 0)$. For our computations we choose $\epsilon = 0.1$, so that the dynamics in the $y$-direction is roughly ten times faster than in the $x$-direction. The potential energy surface is shown in Figure 3.19 together with equilibrium probability density function for $\beta = 1$.

The key for understanding the reaction is to realize that the important barriers for the dynamics are the barriers in the $y$-direction. Suppose we fix an $x = x_0$ and consider the restricted potential $V(x_0, y)$, which then only depends on $y$. Due to the separation of time scale, this is the potential that the $y$-variable effectively feels while the $x$-variable is quasi-frozen and evolving only on a longer time scale. Consider the energy barriers for different $x_0$ in $V(x_0, y)$; denoting these barriers by $\Delta V(x_0)$, it

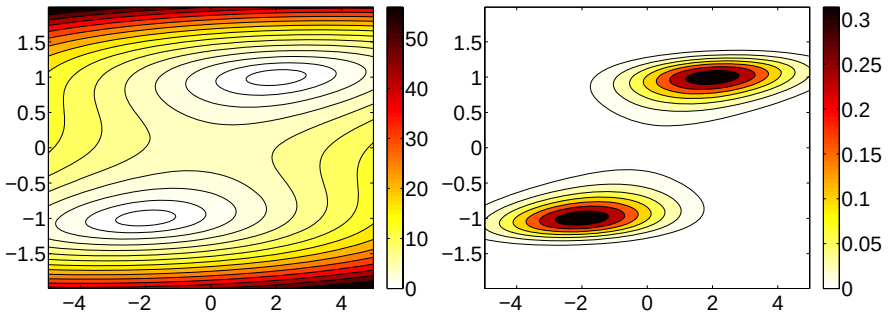


Figure 3.19.: Left: Contour plot of the potential (3.48). Right: Contour plot of Boltzmann-Gibbs equilibrium probability density function. Results for $\beta = 1$.

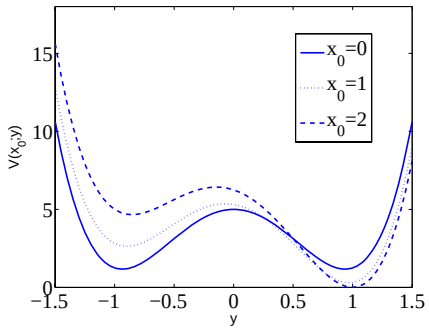


Figure 3.20.: The potential $V(x_0, y)$ of the fast-slow example as a function of $y$ for $x_0 = 0$, $|x_0| = 1$ and $|x_2| = 2$. Thus, the barrier to overcome increases as $|x_0|$ increases.

can be seen that $\Delta V(x_0)$ attains a local maximum at $x_0 = 0$, and decreases as $|x_0|$ increases which is illustrated in Figure 3.20.

Because of this feature, one expects that the reactive trajectories will tend to wait near the reactant state $A$ until they reach a fiber in the $y$-direction with a low barrier $\Delta V(x_0)$ to hop over. Since there is two groups of such fibers on either sides of the $y$-axis, there should be two predominantly vertical reaction channels. Let us now confirm this intuitive picture via TPT.

The contour plot of the committor function is shown in Figure 3.21. Consistent with the separation of time-scale it shows that the isocommittor surfaces are predominantly vertical except in a narrow strip around the $x$-axis.

A typical reactive trajectory is shown in the left panel of Figure 3.22. Consistent with the intuitive picture given above, because of the separation of time-scale, the trajectory spends a relatively long amount of time in the vicinity of the states $A$ and $B$ and a relatively short amount of time transiting between these states (the latter motion being predominantly in the fast $y$-direction). As explained in the previous example, this behavior of the dynamics affects the probability density function of the reactive trajectories which is peaked in the regions where the trajectories spend most time. The right panel of Figure 3.22 shows this effect. The probability density function $\rho_{AB}(x)$ is bimodal and attains local maxima in regions close to the states

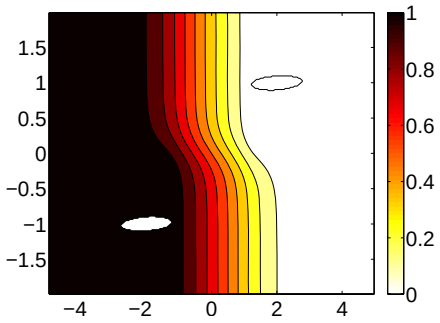


Figure 3.21.: Contour plot of the isocommittor function for the fast-slow example with $\beta = 1$ and $\epsilon = 0.1$.

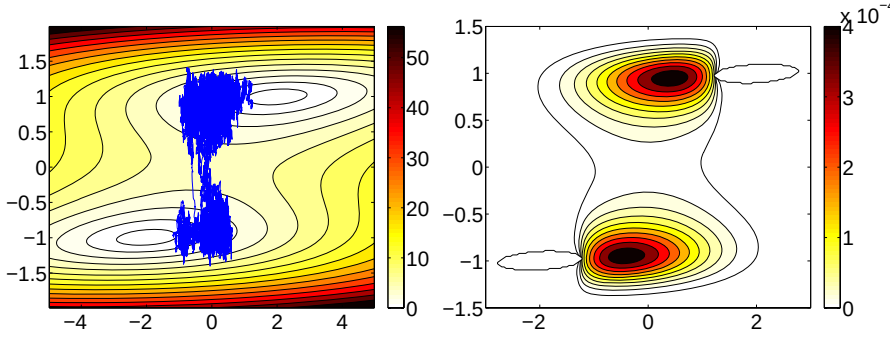


Figure 3.22.: Left: A typical reactive trajectories in (3.47). Right: Probability density function of reactive trajectories. Results for $\beta = 1$ and $\epsilon = 0.1$.

$A$ and $B$. Notice that $\rho_{AB}(x)$ does not give much information about the reaction channels.

To visualize the reaction channels we proceed similarly as in the previous examples and choose the dividing surface $S = \{(x, 0) : -1.5 \leq x \leq 1.5\}$ to compute the intensity of the probability current used to color the streamlines of this current. The results are shown in Figure 3.23. Consistent with the intuitive picture given above, there are two predominantly vertical channels. Notice that most of the flux across $S$ goes either at the left or the right of the saddle point.

Finally, the reaction rates predicted by TPT and computed by DNS are given in Table 3.5.

This example illustrates the subtle effects that time-scale separation may have on the reaction pathway and shows that TPT is able to capture these effects.

| | |
|---|---|
| $k_{AB}$ via (3.38) | $3.278 \cdot 10^{-2}$ |
| $k_{AB}$ via (3.39) | $3.239 \cdot 10^{-2}$ |
| $k_{AB}$ via DNS | $(3.189 \pm 0.076) \cdot 10^{-2}$ |

Table 3.5.: Reaction rate computed for the fast-slow potential at $\beta = 1$. Results of DNS based on $N = 10^5$ reactive trajectories.

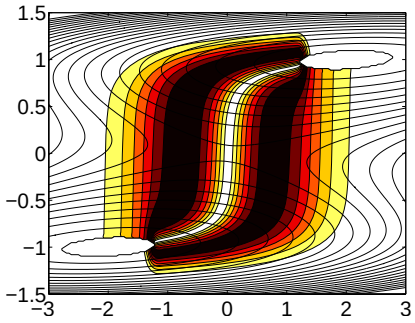


Figure 3.23.: Streamlines of the probability current colored according to the intensities on the dividing surface $S = \{(x, 0) : -1.5 \leq x \leq 1.5\}$. Result for $\beta = 1$.

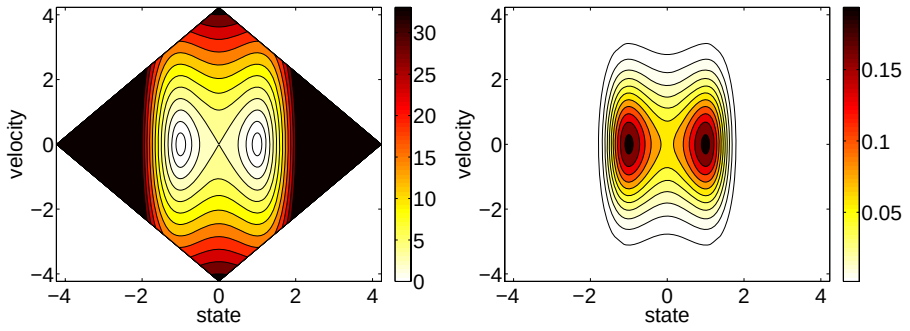


Figure 3.24.: Left: The contour plot shows the Hamiltonian $H(x, v)$ associated with the double-well potential in (3.49). Right: Contour plot of the Boltzmann-Gibbs equilibrium probability density function $Z^{-1}e^{-\beta H(x,v)}$. Results for $\beta = 1$.

## 3.9. Langevin Dynamics

In this section we apply TPT to an example of the Langevin equation (3.31). Before we present in detail our numerical experiments, we want to point out again, that we can not analytically guarantee the differentiability of the forward and backward committor function as a solution of a hypoelliptic, mixed-boundary value problem of the form in A.3. However, the following numerical results show that for the particular choice of the domain $\Omega$ and the parameters of the Langevin dynamics the committor functions are sufficiently smooth.

Here we assume that $(x, v) \in \mathbb{R} \times \mathbb{R}$ and we set $\gamma_1 = m_1 = 1$ (Notice that if the mass is equal to one, the momentum is identical with the velocity of the particle). We also assume that the potential is the double-well potential given by

$$V(x) = (x^2 - 1)^2 \tag{3.49}$$

with minima at $x = -1$ and $x = 1$ and a local maximum at $x = 0$. In Figure 3.24 we show the Hamiltonian function $H(x, v)$ associated with the double-well potential in (3.49) and the Boltzmann-Gibbs equilibrium probability density function for $\beta = 1$. Although the structure of the potential is very simple, it allows us to illustrate how

| | $k_{AB}$ via DNS | $k_{AB}$ via (3.39) | $k_{AB}$ via (3.38) |
|---|---|---|---|
| $\gamma = 1$ | $(3.833 \pm 0.061) \cdot 10^{-2}$ | $3.778 \cdot 10^{-2}$ | $3.721 \cdot 10^{-2}$ |
| $\gamma = 2$ | $(4.019 \pm 0.171) \cdot 10^{-2}$ | $3.918 \cdot 10^{-2}$ | $3.898 \cdot 10^{-2}$ |
| $\gamma = 5$ | $(2.634 \pm 0.106) \cdot 10^{-2}$ | $2.523 \cdot 10^{-2}$ | $2.483 \cdot 10^{-2}$ |
| $\gamma = 10$ | $(1.534 \pm 0.032) \cdot 10^{-2}$ | $1.460 \cdot 10^{-2}$ | $1.361 \cdot 10^{-2}$ |

Table 3.6.: Reaction rates computed for several friction coefficients via DNS of the Langevin dynamics and via TPT using (3.39) or (3.38). All computations are done for the same temperature $\beta = 1$.

the reaction pathway depends on the friction constant $\gamma$. Keeping the temperature constant, we study three different scenarios: the high, medium and low friction cases. For reasons of numerical stability we have to introduce a coordinate transformation which amounts to rotate the mesh by $\pi/4$ and solve the committor equation (3.32) on this mesh, see Appendix: Section A.1.3. This explains our unusual choice of the diamond-shaped domain $\Omega$ as visible in Figure 3.24. The reactant state $A$ and the product state $B$ are determined in a similar way as in the previous section, i.e., their union include all states $(x, v)$ with $H(x, v) < 1$.

Before we start with a detailed description of the reaction pathways, we state the reaction rates in Table 3.6 computed for different friction coefficients via TPT and compare them with those obtained via direct numerical simulation of the Langevin dynamics (3.31). As one can see in Table 3.6 the rates agree within numerical error.

### 3.9.1. High Friction Case, $\gamma = 10$

As mentioned in Section 2.1.10, Langevin leads to Smoluchowski dynamics in the high friction limit $\gamma \to \infty$. In the present case, the overdamped equation is the one-dimensional equation

$$\dot{x}(t) = 4\gamma^{-1}(x(t) - x^3(t)) + \sqrt{2\beta^{-1}\gamma^{-1}}\,\eta(t) \tag{3.50}$$

Since (3.50) involves the position $x(t)$ but not the velocity $v(t)$, in this limit the probability to reach the set $B$ before the set $A$ conditional on starting at point $(x_0, v_0)$ must be independent of the velocity $v_0$. In other words, for large enough $\gamma$, $q(x, v) \approx q(x)$ where $q(x)$ is the committor function of (3.50) and the level sets of the committor function are (almost) parallel to the velocity axis. This is confirmed by the results shown in Figure 3.25. The little deviations near the upper and lower corners are due to the Neumann boundary conditions which forces the level sets of the committor function to be perpendicular to the boundaries. Notice that $q(x, v) \approx q(x)$ also implies that $q_b(x, v) \approx 1 - q(x)$. This is also confirmed by the results shown in Figure 3.25.

The left panel of Figure 3.26 is a contour plot of the probability density function of reactive trajectories $\rho_{AB}(x, v)$. This density is peaked around the saddle point of the Hamilton function $H(x, v)$ at $(x, v) = (0, 0)$ and only shows a slight up-down asymmetry, consistent with the velocity playing no role in the mechanism of the reaction. In the right panel of Figure 3.26 we show the streamlines of the probability current (3.37) of reactive trajectories colored as in the previous example in function

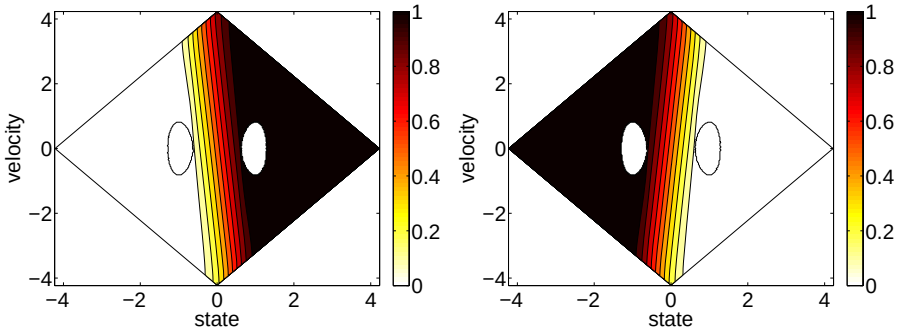


Figure 3.25.: Left: Contour plot of the committor function $q(x, v)$. Right: Contour plot of the backward committor function $q_b(x, v) = 1-q(x, -v)$. Results for $\beta = 1$, $\gamma = 10$.

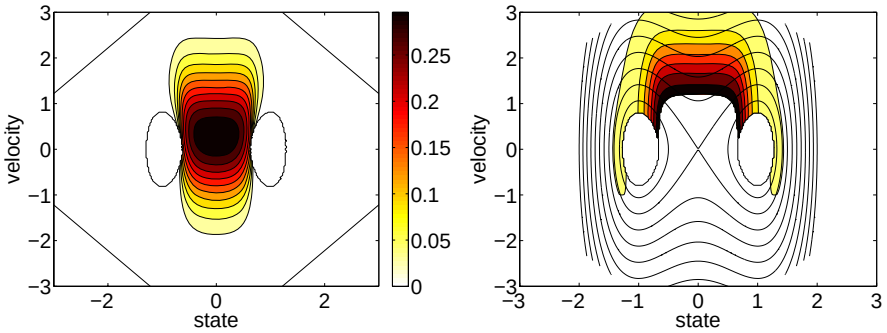


Figure 3.26.: Left: Probability density function of reactive trajectories $\rho_{AB}(x, v)$. Right: Reaction tube based on streamlines of the probability current colored according to the intensity of the probability current on the dividing surface $S = \{(0, v) : -3 \leq v \leq 3\}$. Results for $\beta = 1, \gamma = 10$.

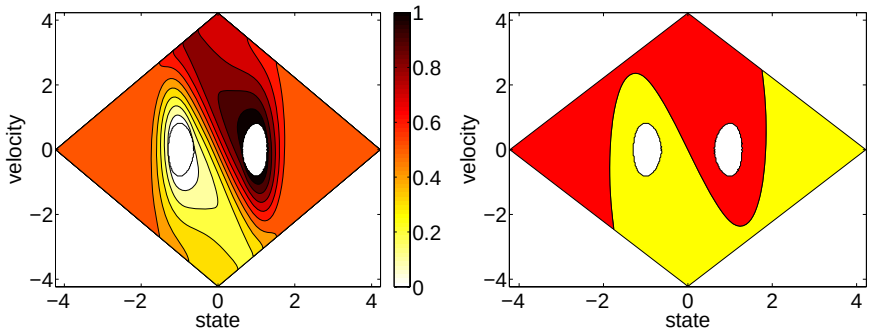


Figure 3.27.: Left: Contour plot of the committor function $q(x, v)$ for $\beta = 1$, $\gamma = 1$. Right: Decomposition of the domain $\Omega$ in phase-space into the two regions $\{(x, v) : q(x, v) < 0.5\}$ (light regime) and $\{(x, v) : q(x, v) > 0.5\}$ (dark regime). The dividing curve is the isocommittor $\frac{1}{2}$ surface where $q(x, v) = \frac{1}{2}$.

of the intensity of the current on $S = \{(0, v) : -3 \leq v \leq 3\}$. The reaction channel is predominantly horizontal.

### 3.9.2. Medium Friction Case, $\gamma = 1$

In the medium friction case, the reaction pathway changes dramatically and now involve the velocity as well as the position. This is apparent from the contour plot of the committor function $q(x, v)$ shown in the left panel of Figure 3.27 and the partition of the domain by the isocommittor $\frac{1}{2}$ surface shown in the right panel. Clearly, the committor function $q(x, v)$ now depends crucially on the velocity, unlike in the high friction case. In fact, the partition of the domain by the isocommittor $\frac{1}{2}$ surface is simple to understand: it is the ghost of the partition of the domain by the deterministic dynamics

$$\begin{cases} \dot{x}(t) = v(t), \\ \dot{v}(t) = -\dfrac{\partial V(x(t))}{\partial x} - \gamma v(t). \end{cases} \tag{3.51}$$

Because $\gamma > 0$ in this equation, every trajectory initiated at a point $(x, v) \in \mathbb{R}^{2d} \setminus (A \cup B)$ will asymptotically end up either in state $A$ or in state $B$. Figure 3.28 shows the partition of phase-space that this induces: the dark grey region contains all the points which end up in $B$ and the light grey region those which end up in $A$. Clearly, the resulting partition is close to the one by the isocommittor function $\frac{1}{2}$ shown in Figure 3.27, which indicates that the temperature is small enough so that it does not really affect this partition, except for wiping out the most external strips in the left and right corner in Figure 3.28 (though this wiping effect is also due to the external boundary conditions imposed when solving for $q(x, v)$ and is less pronounced in the low friction case, see Figure 3.31). Of course, in the absence of noise, there is no reaction, so the noise-free Langevin equation (3.51) is limited in the information that it can provide about the reaction and the full arsenal of TPT remains necessary to understand it.

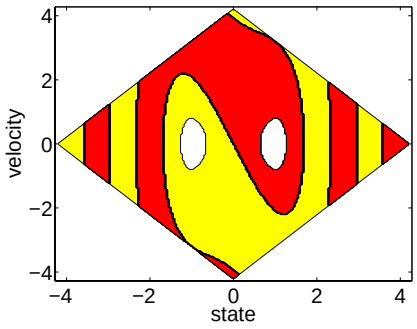


Figure 3.28.: Partition into regions that are asymptotically attracted to sets $A$ or $B$, respectively, for the noise free Langevin equation (3.51). Notice the similarity in the core with the partition by the isocommittor $\frac{1}{2}$ surface shown in the right panel in Figure 3.27.

The probability density function of reactive trajectories $\rho_{AB}(x, v)$ is shown in Figure 3.29. As expected we observe that the distribution is peaked around a point with $x = 0$ and $v > 0$, that is, around the maximum of the potential but in the region of positive velocities since these are needed to go from $A$ to $B$.

The reaction tube from $A$ to $B$ is shown in Figure 3.30. This tube too indicates that the reaction pathway is asymmetric in the velocity (and in particular the reaction from $A$ to $B$ studied here is different from the one from $B$ to $A$ – the reaction tube for the latter can be visualized by flipping Figure 3.30 upside-down, that is, by reverting the velocity.)

### 3.9.3. Low Friction Case, $\gamma = 0.001$

When the friction is as low as $\gamma = 0.001$, Langevin dynamics is now close to Hamiltonian dynamics. Nevertheless, at sufficiently long time scales the damping will force the dynamics to get attracted to the vicinity of the minima of the energy landscape which lie inside the states $A$ and $B$, and the noise will eventually induce reactions between these states. Figure 3.31 shows the committor function $q(x, v)$ and the decomposition of the domain into the two regions $\{(x, v) : q(x, v) < 0.5\}$ and $\{(x, v) : q(x, v) > 0.5\}$ (dark grey) in the low friction case. Figure 3.32 shows the probability density function of reactive trajectories $\rho_{AB}(x, v)$ and the reaction tube. In the present case, the streamlines of the probability current of the reactive trajectories (not shown) are very winding around the states $A$ and $B$ and turn out to be difficult to compute accurately.

### 3.9.4. Rough Potential Landscape

In the last example, we study the Langevin dynamics ($\beta = 1, \gamma = 1$) in a perturbed double-well potential given by

$$\tilde{V}(x) = (x^2 - 1)^2 + \sum_{k=1}^{n} \big[a_k \cos(kx) + b_k \sin(kx)\big], \tag{3.52}$$

where the real coefficients $a_k, b_k, k = 1, \ldots, n$ are drawn from a normal distribution $\mathcal{N}(0, \delta^2)$ with variance $\delta^2$ and mean zero. For our numerical example we chose $n = 20$

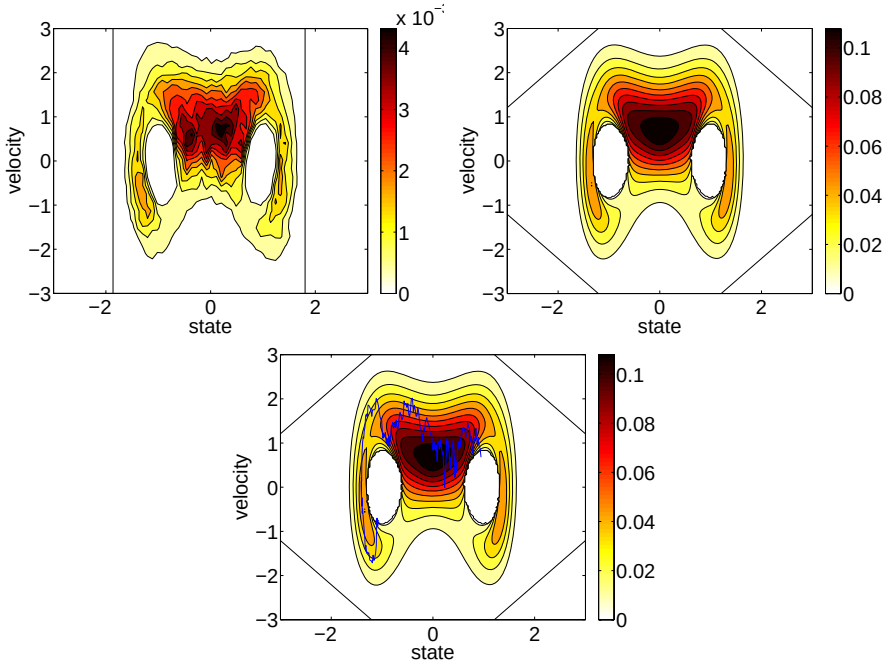


Figure 3.29.: Contour plot of the probability density function of reactive trajectories $\rho_{AB}(x, v)$ when $\beta = 1$, $\gamma = 1$. Top left: Result via DNS based on 300 reactive trajectories and a $40 \times 40$ box decomposition of the domain. Top right: Results from TPT. Bottom middle: A typical reactive trajectory embedded into the contour plot of $\rho_{AB}(x, v)$

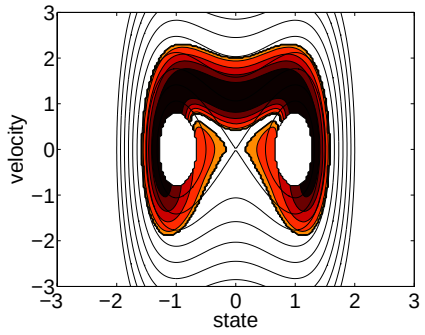


Figure 3.30.: Reaction tube based on streamlines of the probability current colored according to the intensity of the probability current on the dividing surface $S = \{(0, v) : -3 \leq v \leq 3\}$. Results for $\beta = 1$, $\gamma = 1$.

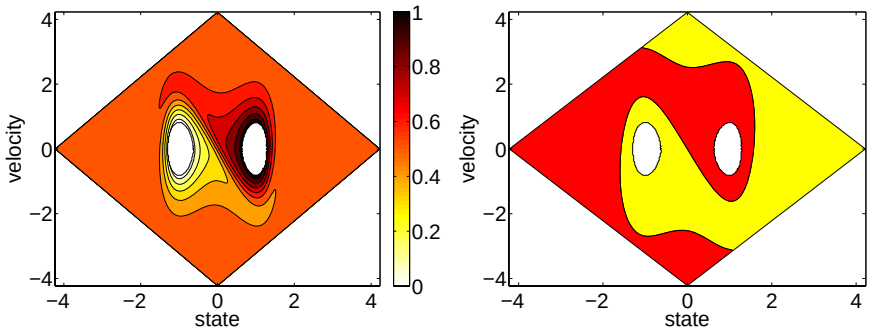


Figure 3.31.: Left: Contour plot of the committor function $q(x, v)$ in the low friction case. Right: Decomposition of the domain into the two regions $\{(x, v) : q(x, v) < 0.5\}$ (light regime) and $\{(x, v) : q(x, v) > 0.5\}$ (dark regime). The dividing curve is the isocommittor $\frac{1}{2}$ surface. Results for $\beta = 1$, $\gamma = 0.001$.

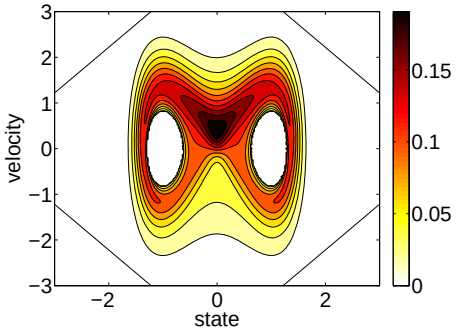


Figure 3.32.: Contour plot of the probability density function of reactive trajectories $\rho_{AB}(x, v)$. Result for $\beta = 1, \gamma = 0.001$.

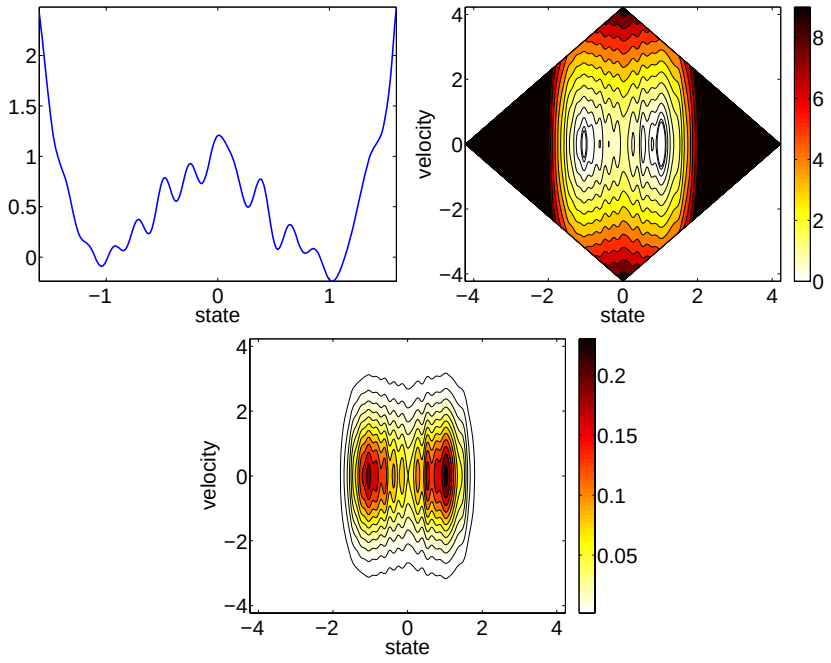


Figure 3.33.: Top left: The graph of the perturbed double-well potential in (3.52). Top right: Contour plot of the Hamiltonian $\tilde{H}(x, v)$ associated with the perturbed double-well potential. Bottom: Contour plot of the Gibbs equilibrium probability density function $\tilde{Z}^{-1}e^{-\beta\tilde{H}(x,v)}$. Results for $\beta = 1$.

and $\delta = 0.01$. In the left top panel of Figure 3.33 we show the graph of the perturbed double-well potential together with the associated Hamiltonian (right top panel) and the associated Gibbs probability density function (bottom panel). To make things comparable, we chose the same mesh discretization of the phase-space domain $\Omega$ and the same sets $A$ and $B$ as in the unperturbed double-well potential case. One can see in the left panel of Figure 3.34 that the level sets of the forward committor function and, in particular, the $\frac{1}{2}$-committor surface (right panel) are rough but their overall shape is more or less comparable to the shape of the level sets depicted in Figure 3.27, respectively. As in opposite to the smooth case, here the probability density function of reactive trajectories $\rho_{AB}(x, v)$ (see top left panel of Figure 3.35) exhibits several peaks which are due to the several local minima in the perturbed potential landscape in which reactive trajectories get trapped on their way from $A$ to $B$. A typical $AB$-reactive trajectory is given in the top right panel of Figure 3.35. Finally, we illustrate the resulting transition tube in the bottom panel of Figure 3.35.

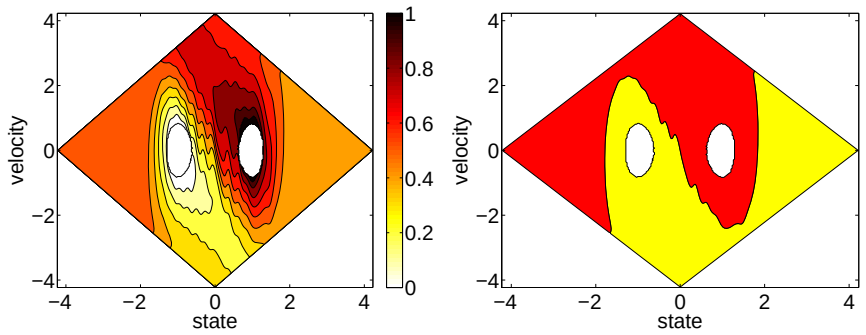


Figure 3.34.: Left: Contour plot of the committor function $q(x, v)$ for $\beta = 1$, $\gamma = 1$. Right: Decomposition of the domain $\Omega$ in phase-space into the two regions $\{(x, v) : q(x, v) < 0.5\}$ (light regime) and $\{(x, v) : q(x, v) > 0.5\}$ (dark regime). The dividing curve is the isocommittor $\frac{1}{2}$ surface where $q(x, v) = \frac{1}{2}$.

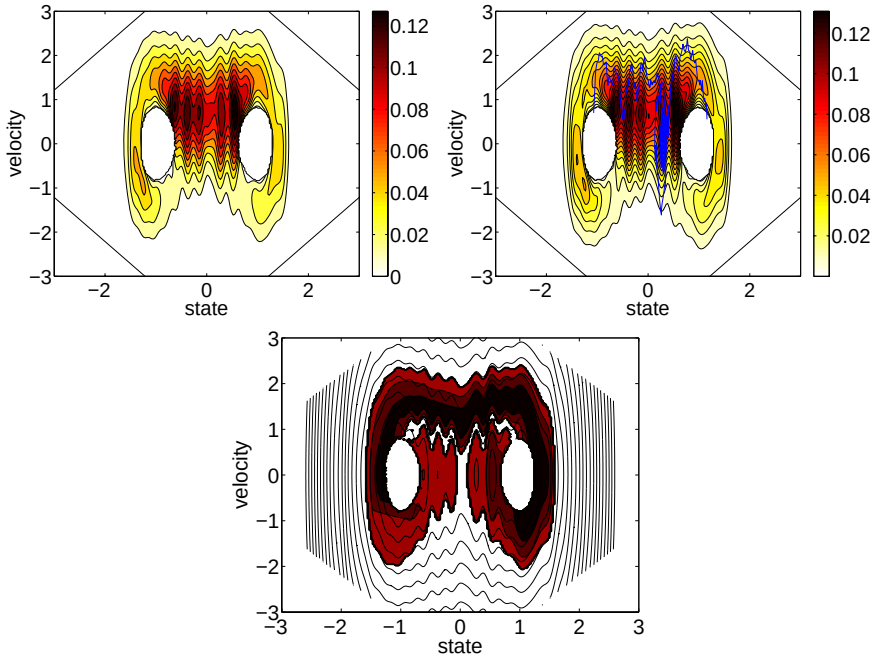


Figure 3.35.: Top left: Contour plot of the probability density function of reactive trajectories $\rho_{AB}(x, v)$. Top right: A typical reactive trajectory embedded in the contour plot of $\rho_{AB}(x, v)$. Bottom middle: Reaction tube based on streamlines of the probability current colored according to the intensity of the probability current on the dividing surface $S = \{(0, v) : -3 \leq v \leq 3\}$. Results for $\beta = 1$, $\gamma = 1$.